



Associated Molecular and Atomic Clouds with X-Ray Shell of Superbubble 30 Doradus C in the LMC

Y. Yamane¹, H. Sano², M. D. Filipović³, K. Tokuda^{2,4}, K. Fujii⁵, Y. Babazaki¹, I. Mitsuishi¹, T. Inoue¹, F. Aharonian^{6,7,8}, T. Inaba¹, S. Inutsuka¹, N. Maxted⁹, N. Mizuno^{2,5}, T. Onishi⁴, G. Rowell¹⁰, K. Tsuge¹, F. Voisin¹⁰, S. Yoshiike¹, T. Fukuda¹, A. Kawamura², A. Bamba^{11,12}, K. Tachihara¹, and Y. Fukui^{1,13}

¹Department of Physics, Nagoya University, Furo-cho, Chikusa-ku, Nagoya 464-8601, Japan; yamane.y@nagoya-u.ac.jp

²National Astronomical Observatory of Japan, Mitaka, Tokyo 181-8588, Japan; hidetoshi.sano@nao.ac.jp

³Western Sydney University, Locked Bag 1797, Penrith South DC, NSW 2751, Australia

⁴Department of Physical Science, Graduate School of Science, Osaka Prefecture University, 1-1 Gakuen-cho, Naka-ku, Sakai 599-8531, Japan

⁵Department of Astronomy, School of Science, The University of Tokyo, 7-3-1 Hongo, Bunkyo-ku, Tokyo 133-0033, Japan

⁶Max-Planck-Institut für Kernphysik, P.O. Box 103980, D-69029 Heidelberg, Germany

⁷Dublin Institute for Advanced Studies, School of Cosmic Physics, 31 Fitzwilliam Place, Dublin 2, Ireland

⁸High Energy Astrophysics Laboratory, RAU, 123 Hovsep Emin Street, Yerevan 0051, Armenia

⁹School of Science, University of New South Wales, Australian Defence Force Academy, Canberra, ACT 2600, Australia

¹⁰School of Physical Sciences, The University of Adelaide, North Terrace, Adelaide, SA 5005, Australia

¹¹Department of Physics, School of Science, The University of Tokyo, 7-3-1 Hongo, Bunkyo-ku, Tokyo 133-0033, Japan

¹²Research Center for the Early Universe, The University of Tokyo, 7-3-1 Hongo, Bunkyo-ku, Tokyo 113-0033, Japan

¹³Institute for Advanced Research, Nagoya University, Furo-cho, Chikusa-ku, Nagoya 464-8601, Japan

Received 2020 May 7; revised 2021 June 11; accepted 2021 June 11; published 2021 September 2

Abstract

30 Doradus C is a superbubble that emits the brightest non-thermal X- and TeV gamma-rays in the Local Group. To explore the detailed connection between the high-energy radiation and the interstellar medium, we have carried out new CO and HI observations using the Atacama Large Millimeter/Submillimeter Array (ALMA), Atacama Submillimeter Telescope Experiment, and the Australia Telescope Compact Array with resolutions of up to 3 pc. The ALMA data of $^{12}\text{CO}(J=1-0)$ emission revealed 23 molecular clouds, with typical diameters of $\sim 6\text{--}12$ pc and masses of $\sim 600\text{--}10,000 M_{\odot}$. A comparison with the X-rays of XMM–Newton at ~ 3 pc resolution shows that X-rays are enhanced toward these clouds. The CO data were combined with the HI to estimate the total interstellar protons. A comparison of the interstellar proton column density and the X-rays revealed that the X-rays are enhanced with the total proton column density. These are most likely to be caused by the shock-cloud interaction, which is modeled by magnetohydrodynamical simulations (Inoue et al. 2012). We also note a trend for the X-ray photon index to vary with distance from the center of the high-mass star cluster. This suggests that the cosmic-ray electrons are accelerated by one or multiple supernovae in the cluster. Based on these results, we discuss the role of the interstellar medium in cosmic-ray particle acceleration.

Unified Astronomy Thesaurus concepts: Cosmic rays (329); Interstellar clouds (834); Superbubbles (1656); Supernova remnants (1667); Radio astronomy (1338)

1. Introduction

30 Doradus C (hereafter 30 Dor C) is one of the brightest synchrotron X-ray and TeV gamma-ray superbubbles in the Local Group, which is noticed from the viewpoint of cosmic-ray acceleration. Le Marne (1968) discovered this superbubble located 200 pc far from the high-mass star-forming region R136 by radio continuum observation. Mills et al. (1984) detected the shell-like structure in the 843 MHz band with a diameter of $\sim 6'$ (~ 80 pc at a distance of Large Magellanic Cloud (LMC) of ~ 50 kpc; Pietrzyński et al. 2013). A similar shell-like structure was also observed in thermal and non-thermal X-ray emissions (e.g., Long et al. 1981; Chu & Mac Low 1990; Dennerl et al. 2001). Non-thermal X-rays in 30 Dor C are bright in the northern and western sides of the shell, and are confirmed to be synchrotron emissions (Bamba et al. 2004; Smith & Wang 2004; Yamaguchi et al. 2009; Kavanagh et al. 2015, 2019; Lopez et al. 2020). Lopez et al. (2020) performed spectral analysis using XMM–Newton and NuSTAR X-ray data, and found the maximum electron energy of $\sim 70\text{--}110$ TeV, assuming B -field strength of $4 \mu\text{G}$. In addition, H.E.S.S. Collaboration et al. (2015) detected gamma-rays from 30 Dor C, whose luminosity is

$(0.9 \pm 0.2) \times 10^{35} \text{ erg s}^{-1}$ at 1–10 TeV. The authors suggested that the energy of the cosmic rays may reach $10^{15.5}$ eV (i.e., “knee” energy) in this superbubble. Accordingly, it is certain that VHE cosmic-rays are accelerated in the superbubble 30 Dor C.

Associated gas with 30 Dor C has been discovered. This superbubble is known as a site of interactions between the shock and the cloudy medium. Sano et al. (2017) (hereafter Paper I) detected molecular clouds associated with 30 Dor C using Mopra in the $^{12}\text{CO}(J=1-0)$ transition (beam size id $\sim 45''$, corresponding a spatial resolution of ~ 11 pc at the distance of the LMC). The authors confirmed that most of the molecular clouds are distributed in the western side of the shell. There is also an OB association LH 90 with ages of 3–4 Myr and 7–8 Myr in the western side of the shell, which is considered to be the parent objects of 30 Dor C (e.g., Testor et al. 1993) and synchrotron X-rays are remarkably bright. Paper I also reported spatial separations of ~ 10 pc between synchrotron X-ray peaks and CO peaks. They argued that these separations could be interpreted as magnetic field amplification around dense clouds by shock-cloud interaction, which was proposed by Inoue et al. (2009, 2012).

Table 1
Observed Parameters

Telescopes	ALMA		ASTE	ATCA	
	Cycle 3	Cycle 5		EW352	6B
Target line	$^{12}\text{CO}(J=1-0)$		$^{12}\text{CO}(J=3-2)$	H I 21 cm	
Beam size (")	$\sim 11 \times 15$		24^a	16^a	
Observing dates	2016/Mar./18, 20	2017/Dec./22, 29, 30	2015/Nov./02, 05, 06	2016/Jan./26	2016/Jan./28
rms noise (K)	~ 0.07	~ 0.05	~ 0.12	~ 8	
Base line (m)	7.3–33.7	8.4–35.4	...	31–4439	214–5969
Velocity resolution (km s^{-1})	0.4		0.5	1.0	
Band width	125 MHz		128 MHz	1 GHz	
Number of channels (channel)	2048		1024	2048	
Total power	yes		...	yes	

Note.

^a Convolved beam size.

Subsequently, Babazaki et al. (2018) executed a spatially resolved X-ray spectral analysis with a scale of ~ 10 pc in 30 Dor C, which led to our understanding of the conditions of X-ray emissions (e.g., photon index, intensity, and absorbed column density). The spatial distribution that divided 30 Dor C into 70 parts shows the spatial anti-correlation between the X-ray photon index and the absorption-corrected intensity. It also shows a tendency for the photon index to be small in the western side, where the intensity is bright. They compared the distribution of the photon index with that of molecular clouds reported by Paper I qualitatively. They suggested the possibility of a connection between the variation of the photon index and the shock-cloud interaction, as seen in Galactic SNR and theoretical results (e.g., Inoue et al. 2009, 2012; Sano et al. 2010, 2013, 2017, 2020). However, there have been no follow up studies because of a lack of the high-sensitivity and high-resolution CO/HI data. Therefore, the mechanism that is responsible for the variation of the X-ray photon index and the intensity is unknown.

In this paper, we present new high-sensitivity and high-resolution data of $^{12}\text{CO}(J=1-0, 3-2)$ and HI emission for the superbubble 30 Dor C using the Atacama Large Millimeter/Submillimeter Array (ALMA), Atacama Submillimeter Telescope Experiment (ASTE), and the Australia Telescope Compact Array (ATCA). Using these data, we intend to reveal the distributions of total interstellar gas (molecular and atomic gas) associated with the superbubble 30 Dor C with a spatial resolution of $\sim 3-6$ pc. In addition, we will investigate the mechanism of cosmic-ray acceleration by the interaction of the cloudy medium with the SN shock through a spatial comparison of the interstellar gas with X-ray photon index, intensity, and absorbing column density. Section 2 introduces observations and reductions of the datasets that we used in this study. Section 3 has five subsections: Section 3.1 describes the spatial distributions of CO, HI, and X-ray; Section 3.2 explains the identification of the CO clouds; Section 3.3 gives velocity structures of CO and HI; finally, Sections 3.4 and 3.5 present the results of spatial comparison of the total proton column density with the spectrum conditions in X-rays. We discuss the results in Section 4 and in Section 5 we summarize the conclusions.

2. Observations and Data Reduction

2.1. CO and HI Data

We newly observed CO and HI data using ALMA, ASTE, and ATCA. The observed parameters are summarized in Table 1. We describe the detailed information for each observation below.

2.1.1. ALMA CO $^{12}\text{CO}(J=1-0)$

We carried out ALMA Band 3 (86–116 GHz) observations of $^{12}\text{CO}(J=1-0)$ emission line toward the northwest of 30 Dor C and MC SNR J0536–6913 during the Cycle 3 semester (Proposal #2015.1.01232, PI: H. Sano). We used the mosaic-mapping mode of a $200'' \times 150''$ region centered at $(\alpha_{J2000}, \delta_{J2000}) = (5^{\text{h}} 35^{\text{m}} 51^{\text{s}}.00, -69^{\circ} 12' 47''.00)$ for the northwest of 30 Dor C, and of a $85'' \times 85''$ region centered at $(\alpha_{J2000}, \delta_{J2000}) = (5^{\text{h}} 36^{\text{m}} 16^{\text{s}}.00, -69^{\circ} 13' 27''.00)$ for the MC SNR J0536–6913. The observations used eight 7 m antennas as interferometer and three 12 m antennas as total-power array. The observations were executed on 2016 March 18 and 20, through five spectral windows. The target molecular line was $^{12}\text{CO}(J=1-0)$ with a bandwidth of 125.0 MHz ($61.035 \text{ kHz} \times 2048 \text{ channels}$). The baselines ranged from 7.3 to 33.7 m, corresponding to $u-v$ distances from 2.8 to 12.9 k λ . The calibration of the complex gains was carried out by observations of J0538–4405, phase calibration on J0601–7036, and flux calibration on J0519–4546.

We also carried out ALMA Band 3 observations of $^{12}\text{CO}(J=1-0)$ emission line toward the southwest of 30 Dor C during the Cycle 5 semester (Proposal #2017.1.01363.S, PI: Y. Yamane). The mosaic-mapping mode was also used to observe $210'' \times 130''$ region centered at $(\alpha_{J2000}, \delta_{J2000}) = (5^{\text{h}} 35^{\text{m}} 50^{\text{s}}.808, -69^{\circ} 12' 21''.96)$. The observations used 11 7 m antennas as interferometer and three 12 m antennas as total-power array. The observations were carried out on 2017 December 22, 29 and 30, with the same spectral setting of Cycle 3 observations. The baselines ranged from 8.4 to 35.4 m, corresponding to $u-v$ distances from 3.2 to 13.6 k λ . The maximum recoverable scale is $\sim 23''.7$ for the 7 m array data. The calibration of the complex gains was carried out using observations of J0522–3627, phase calibration on J0529–7245, and flux calibration on J0516–6207.

For the imaging process from the visibility data, we used the Common Astronomy Software Applications package (CASA, version 5.1.0; McMullin et al. 2007). We combined 7 m array

Table 2
XMM-Newton Observations used in the Analysis

Obs. ID	R.A. (deg.)	Decl. (deg.)	Obs. Date	Exposure (ks)			Orbit	PI Name
				MOS1	MOS2	PN		
0104660301	83.866666	−69.269722	2000–11–25	20.9	20.2	...	177	Watson
0144530101	83.866666	−69.269750	2003–05–10	47.4	47.4	...	626	McCray
0406840301	83.866666	−69.269750	2007–01–17	75.3	77.1	61.1	1302	Haberl
0506220101	83.867916	−69.270278	2008–01–11	82.1	84.7	70.8	1482	Haberl
0556350101	83.867916	−69.270278	2009–01–30	80.4	83.3	66.5	1675	Haberl
0601200101	83.867916	−69.270278	2009–12–12	87.6	87.3	82.5	1833	Haberl
0650420101	83.867916	−69.270278	2010–12–12	58.2	61.7	52.8	2016	Haberl
0671080101	83.867916	−69.270278	2011–12–02	68.8	70.0	64.1	2194	Haberl
0690510101	83.867916	−69.270278	2012–12–11	14.7	67.2	59.5	2382	Haberl
0743790101	83.867916	−69.270278	2014–11–29	64.3	66.5	56.3	2742	Haberl
0763620101	83.867916	−69.270278	2015–11–15	62.3	62.8	57.9	2918	Haberl

Note. All exposure times indicate so called “Good time interval (GTI)”. The target name for all observations was SN 1987A.

data taken in both the Cycle 3 and 5 semesters. We applied the natural weighting to recover the weak extended emission. We also applied the multi-scale CLEAN algorithm implemented in CASA (Cornwell 2008). The multi-scale CLEAN approach is useful because it can better restore the extended emission and reduce negative structures. Finally, we combined the cleaned 7 m array data with the total-power data using feather task implemented in CASA. The synthesized beam size was $\sim 11'' \times 15''$ with a position angle of $66^\circ.1$, corresponding a spatial resolution of $\sim 2.7 \times 3.6$ pc at the LMC distance ~ 50 kpc. The rms noise fluctuations of the data taken in the Cycle 3, and Cycle 5 were ~ 0.07 K, and ~ 0.05 K, respectively, with a velocity resolution of 0.4 km s^{-1} .

2.1.2. ASTE CO $^{12}\text{CO}(J=3-2)$

Observations of $^{12}\text{CO}(J=3-2)$ line emission were conducted by the ASTE (Ezawa et al. 2004) during 2015 November (Proposal#AC152006, PI: H. Sano). We used the on-the-fly mode with Nyquist sampling, and the mapping area was $7'.5 \times 7'.5$ centered on the position of $(\alpha_{J2000}, \delta_{J2000}) = (5^{\text{h}} 36^{\text{m}} 00^{\text{s}}, -69^\circ 11' 42'')$. The frontend was a 2SB SIS mixer receiver called “DASH 345.” The typical system temperature was 250 K in the single side band. The backend was the digital spectrometer, “MAC” (Sorai et al. 2000), which had a velocity resolution of $\sim 0.11 \text{ km s}^{-1}$ per channel and coverage of $\sim 111 \text{ km s}^{-1}$ at 350 GHz. The pointing accuracy was checked every 2 hr and the measurements were kept within an error of $2''$. The intensity calibration was applied by observing N159W $[(\alpha_{J2000}, \delta_{J2000}) = (5^{\text{h}} 39^{\text{m}} 37^{\text{s}}, -69^\circ 45' 32'')]$ (Minamidani et al. 2011). The beam size was $22''$ and we adopted a grid spacing of $7'.5$ in these observations. In this study, data were smoothed with a Gaussian kernel to an effective beam size of $24''$. The final noise fluctuations were ~ 0.12 K at the velocity resolution of 0.5 km s^{-1} .

2.1.3. ATCA HI

We used the HI 21 cm data that were obtained with ATCA and the Parkes radio telescope. The observations by ATCA were carried out using two configurations on 2016 January 26 (EW352), and on 2016 February 28 (6B) (Proposal#C3070, PI: K. Fujii). The baseline ranges of these configurations are from 31 to 4439 m for EW352 and from 214 to 5969 m for 6B. The calibration was carried out by observations of PKS 1934–638 as flux and bandpass calibrator, and PKS 0530–727

as phase calibrator. For our ATCA data reduction, we used Miriad software (Sault et al. 1995). The best HI images were obtained using neutral weighting scheme of $\text{robust} = 0$ and self-calibration. To recover the diffuse emission, we combined the HI data with the previous HI survey data of the whole LMC presented by Kim et al. (2003), which were obtained using ATCA and the Parkes single-dish telescope. We used IMMERGE task, which feathers together (a linear merging process) the total-power corrected image by Kim et al. (2003) and the present interferometer-only image. The combined HI image has an angular resolution of $12''.24 \times 10''.90$ with a position angle of $45^\circ.2$. In this study, the data were smoothed with a Gaussian kernel to an effective beam size of $16''$. The final noise fluctuation was ~ 8 K at the velocity resolution of 1.0 km s^{-1} .

2.2. XMM-Newton X-rays

30 Dor C was observed by the XMM-Newton EPIC detectors with a total of 15 pointings as of 2017 February. To improve the imaging quality, we omitted observations that had an effective exposure time (good time interval; GTI) less than 10 ks and were not centered on SN 1987A. The final datasets that we have used in this paper are listed in Table 2. We analyzed both the EPIC-MOS and EPIC-pn by using the HEASoft version 6.18 and the XMM-Newton Science Analysis System (SAS Gabriel et al. 2004) version 16.0. For the imaging analysis, we used the XMM-Newton extended source analysis software (ESAS: Kuntz & Snowden 2008). We applied the standard calibration and filtering routines using the SAS tasks *emchain/epchain* and ESAS tasks *mos-filter/pn-filter*. The *pn-spectra/mos-spectra* and *pn-back/mos-back* tasks were used to create the event, exposure, and quiescent particle background (QPB) background images in the 0.3–1.0 keV, 1.0–2.0 keV, 2.0–7.0 keV, and 0.3–7.0 keV in the energy bands for each detector. Finally, we used *merge_comp_xmm* task to create the mosaicked event, exposure, and QPB background images. The adaptive smoothing task *adapt merge* was also applied so that the signal to noise ratio is at least 300 with the pixel size of $\sim 2''$. The combined mosaic images for each energy band are shown in Figure 1(a).

2.3. Planck/IRAS Dust Opacity

We also utilized the archival datasets of the dust opacity at 353 GHz τ_{353} and dust temperature T_d , which were provided by

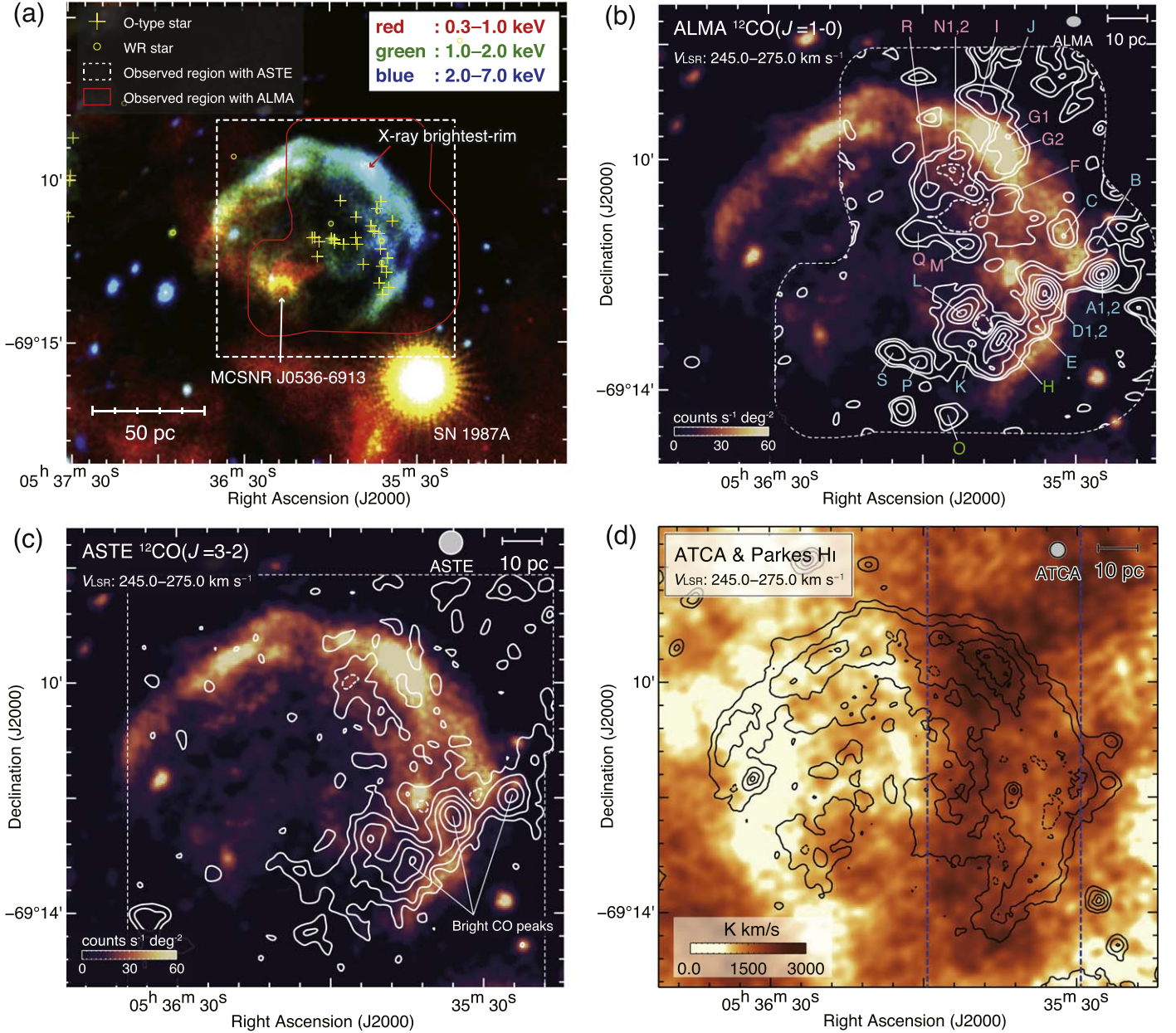


Figure 1. (a) Three-color XMM-Newton EPIC image of 30 Dor C. Red, green, and blue correspond to the energy bands of 0.3–1.0 keV (soft), 1.0–2.0 keV (medium), and 2.0–7.0 keV (hard), respectively. The white-dashed line and red-solid line show the observed areas of ASTE and ALMA, respectively. Yellow crosses and circles indicate positions of O-type stars and WR stars, respectively. MCSNR J0536–6913 and SN 1987A are also shown. (b) Integrated intensity map of ALMA $^{12}\text{CO}(J=1-0)$ superposed on the hard X-ray image. The velocity range is from 245 to 275 km s^{-1} . The region enclosed by the dashed line indicates the observed region with ALMA. Contour levels are 1.03 ($\sim 5\sigma$), 2.07, 5.16, 10.3, 17.6, 26.9, and 38.2 K km s^{-1} . The CO clouds A–S are also indicated. The blue, green, and red labels represent molecular clouds whose peak velocity includes velocity ranges of 245–255 km s^{-1} , 255–265 km s^{-1} , and 265–275 km s^{-1} , respectively. (c) Integrated intensity map of ASTE $^{12}\text{CO}(J=3-2)$ superposed on the hard X-ray image. The velocity range is the same as in (b). Contour levels are 2.46 ($\sim 12\sigma$), 4.51, 8.26, 13.1, and 18.9 K km s^{-1} . The dashed-rectangular region indicates the observed region with ASTE. The bright CO peaks are also shown. (d) Integrated intensity map of ATCA & Parkes HI overlaid with the hard X-ray contours. The velocity range is the same as in (b). Contour levels are 5.0, 10, 25, 50, and 85 $\text{counts s}^{-1} \text{deg}^{-2}$. The vertical-dashed lines indicate the integration range of a position–velocity diagram in Figure 4. The resolutions are indicated in the top right-hand corner of each figure.

using the combined Planck/IRAS data with the graybody fitting (for details, see Planck Collaboration et al. 2014). The datasets are used to compare with the HI data. The angular resolution is $5''.0$ (~ 75 pc at the LMC) with a grid spacing of $2''.4$. For a comparison between τ_{353} and HI, we set the resolution and grid size of HI to that of τ_{353} . Note that the beam size of the data is roughly equal to the spatial extent of 30 Dor C.

3. Results

3.1. Overview of the CO, HI, and X-ray Distributions of 30 Doradus C

We first present the CO, HI, and X-ray distributions of the superbubble 30 Dor C obtained with ASTE, ALMA, ATCA & Parkes, and XMM-Newton. Figure 1(a) shows a three-color X-ray image of 30 Dor C. We found an elliptical shell-like structure of ~ 80 pc in diameter, which is consistent with the previous X-ray studies (e.g., Dennerl et al. 2001; Bamba et al.

2004; Kavanagh et al. 2015; Babazaki et al. 2018). The X-ray shell contains MCSNR J0536–6913 at the position of $(\alpha_{J2000}, \delta_{J2000}) \sim (5^{\text{h}} 36^{\text{m}} 17^{\text{s}}.0, -69^{\circ} 13' 28''.0)$ (Kavanagh et al. 2015; Bozzetto et al. 2017). The hard X-rays (blue: 2.0–7.0 keV) are enhanced in the western shell, while the soft X-rays (red: 0.3–1.0 keV) are bright in the eastern shell. The soft X-rays are originated by thermal plasma, whereas the hard X-rays are dominated by the synchrotron radiation (e.g., Bamba et al. 2004). Hereafter, we refer to the soft X-rays as “thermal X-rays” and the hard X-rays as “synchrotron X-rays.” We also refer to the brightest X-ray peak at $(\alpha_{J2000}, \delta_{J2000}) \sim (5^{\text{h}} 35^{\text{m}} 46^{\text{s}}.5, -69^{\circ} 9' 38''.4)$ as the “X-ray brightest-rim.” It should be noted that 26 O-type stars and six WR stars are distributed in the western side of 30 Dor C.

Figure 1(b) shows the distribution of ALMA $^{12}\text{CO}(J=1-0)$ superposed with the synchrotron X-ray image obtained with XMM-Newton. We select the integration velocity range from 245 to 275 km s^{-1} , which is roughly consistent with the velocity range to be associated with 30 Dor C, as mentioned by Paper I. The observed area is only the western half of the shell, where $^{12}\text{CO}(J=1-0)$ emission was significantly detected by Mopra (see Paper I). We also show CO clouds A–S that will be detailed in Section 3.2. We find bright CO peaks toward the southwest of the shell, which likely corresponding to MC1 and MC2 identified by Paper I (CO clouds A1, A2, D1, D2, and H). These CO peaks show a good spatial anti-correlation with the synchrotron X-ray peaks. We also identified the CO clouds toward the X-ray brightest-rim, corresponding to MCs 3–5 identified by Paper I (e.g., CO clouds G1, and G2). Other CO clouds are also located near the synchrotron X-ray shell (e.g., CO clouds B, C, E, F, I–N, and R).

Figure 1(c) shows the integrated intensity contours of the ASTE $^{12}\text{CO}(J=3-2)$ superposed on the same X-ray image, as shown in Figure 1(b). Molecular clouds appear along the western side of the X-ray shell, whereas there are no dense clouds in the eastern side. We find three bright CO peaks toward the southwest of 30 Dor C, which are nicely rim-brightened in synchrotron X-rays. We also identified the diffuse CO clouds toward the X-ray brightest-rim. The distribution of $^{12}\text{CO}(J=3-2)$ emission is roughly consistent with that of the $^{12}\text{CO}(J=1-0)$ emission, except for the northwestern shell where $^{12}\text{CO}(J=3-2)$ emission is weaker than $^{12}\text{CO}(J=1-0)$ emission.

Figure 1(d) shows the integrated intensity map of the ATCA & Parkes HI overlaid on the XMM-Newton X-ray contours. The HI emission in the western shell is roughly ~ 2 times brighter than that in the eastern shell. The X-ray brightest-rim spatially coincides with the HI peak named “NW cloud” (see also Paper I). No significant absorption features of HI spectra are found toward the eastern shell, which indicates that the low HI brightness temperature means that there is a poor atomic gas environment.

3.2. Physical Properties of the CO Clouds

We here present how to derive physical properties of CO clouds. First, we identified CO clouds associated with 30 Dor C using the ALMA $^{12}\text{CO}(J=1-0)$ data. The procedure of defining a CO cloud is as follows (see also Figure 2):

1. In the CO integrated intensity map over the whole velocity range 245.0 km s^{-1} –275.0 km s^{-1} ($W_0(\text{CO})$ see Figure 1(b)), find a peak of $W_0(\text{CO})$ greater than 5.16

K km s^{-1} [equal to the 25σ level of the ALMA $^{12}\text{CO}(J=1-0)$ data] and define it as an individual integrated intensity peak ($W_0(\text{CO})$ peak).

2. If the $W_0(\text{CO})$ peak is weaker than 5.16 K km s^{-1} , then we only identify it as an individual $W_0(\text{CO})$ peak when the contour of 2.07 K km s^{-1} [equal to the 10σ level] peak has an equivalent diameter over $\sim 30''$.
3. When the separation between a $W_0(\text{CO})$ peak and surrounding peaks is less than $15''$ [equal to the beam size of ALMA $^{12}\text{CO}(J=1-0)$] and the velocity difference of these peaks is less than 4 km s^{-1} , then we regard them as one peak.
4. When a $W_0(\text{CO})$ peak spectrum has a double-peaked profile, then each velocity component is considered to belong to different clouds if the velocity difference is larger than 4 km s^{-1} , which is ~ 2.5 times larger than the typical line width of a cloud. We divide the spectra into two components at the velocity of the minimum intensity between the two peaks.
5. Peak radiation temperature T_R^* , central velocity V_{peak} , and full-width at half-maximum line width ΔV are measured by fitting each spectrum at the $W_0(\text{CO})$ peak by a single Gaussian profile.
6. Maps of a narrow range integrated intensity ($W_g(\text{CO})$) are made around each $W_0(\text{CO})$ peak, whose velocity range is determined from the line width of each spectrum. The surface area A and the position of each cloud are defined as an area enclosed by 5σ contours in the $W_g(\text{CO})$ map and the position of the $W_g(\text{CO})$ peak, respectively.

As a result, we identified individual 23 CO clouds A–S; as shown in Figure 1(b). The physical properties of these clouds are summarized in Table 3. T_R^* ranges from 1.6 to 7.5 K. The typical ΔV is ~ 2 –6 km s^{-1} and the cloud size is ~ 5 –12 pc. We also calculated the CO-derived mass M_{CO} using the following equation:

$$M_{\text{CO}} = m_H \mu \sum_i [D^2 \Omega N_i(\text{H}_2)], \quad (1)$$

where m_H is the mass of hydrogen atom, μ is the mean molecular weight relative to hydrogen atom, D is the distance to the source in unit of cm, equal to 50 kpc, Ω is the solid angle subtended by a unit grid spacing of a square pixel ($0''.5 \times 0''.5$), and $N_i(\text{H}_2)$ is the hydrogen molecule column density for each pixel in unit of cm^{-2} . We adopt $\mu = 2.7$ to take into account the $\sim 36\%$ abundance by mass of helium relative to hydrogen molecule. We also used the following relationship between the hydrogen molecule column density $N(\text{H}_2)$ and the $^{12}\text{CO}(J=1-0)$ integrated intensity $W(\text{CO})$ from Fukui et al. (2008):

$$N(\text{H}_2) = 7.0 \times 10^{20} \cdot W(\text{CO})(\text{cm}^{-2}), \quad (2)$$

where the units for $W(\text{CO})$ are K km s^{-1} . Finally, we obtained the typical M_{CO} of ~ 400 –9000 M_{\odot} and the density of ~ 100 –200 cm^{-3} assuming a spherical shape. Note that the mass, $N(\text{H}_2)$, and density for each cloud are thought to have $\sim 30\%$ relative errors due to uncertainties in Equation (2) (cf. Bolatto et al. 2013).

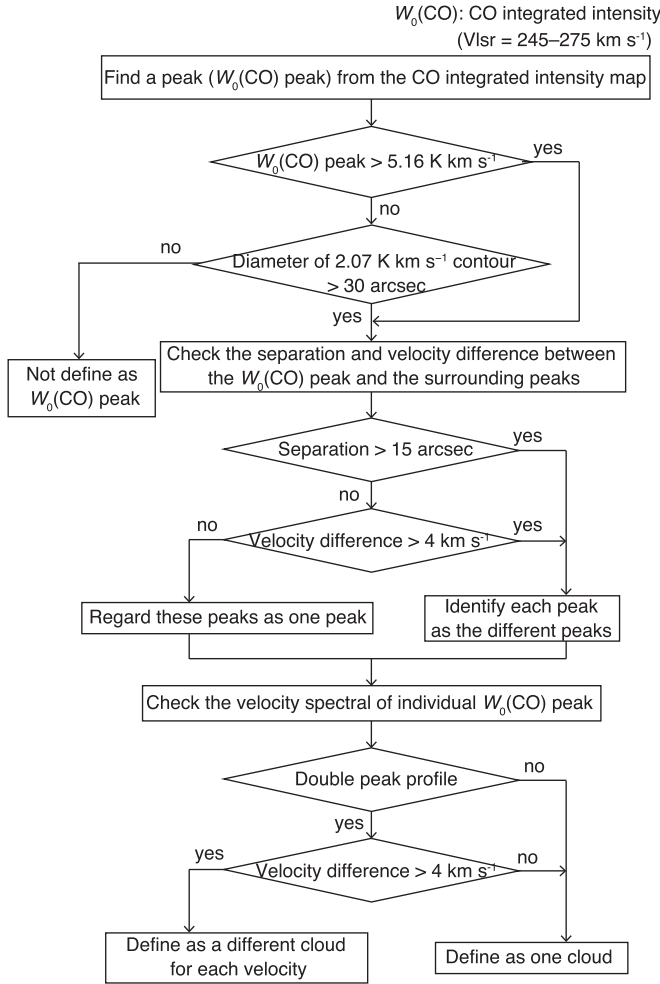


Figure 2. Flowchart of the identification of molecular clouds toward 30 Dor C.

3.3. Velocity Structures of CO and HI Clouds

Figure 3 shows the velocity channel distributions of $^{12}\text{CO}(J=1-0)$, $^{12}\text{CO}(J=3-2)$, and HI overlaid with the XMM-Newton X-ray contours. For the ALMA $^{12}\text{CO}(J=1-0)$, the CO clouds at $V_{\text{LSR}} = 245\text{--}265\text{ km s}^{-1}$ are located in the southwestern shell, while other molecular clouds at $V_{\text{LSR}} = 265\text{--}275\text{ km s}^{-1}$ are distributed in the northwestern shell. The distributions of the ASTE $^{12}\text{CO}(J=3-2)$ are roughly consistent with that of the ALMA $^{12}\text{CO}(J=1-0)$, except for the northwestern clouds at $V_{\text{LSR}} = 265\text{--}275\text{ km s}^{-1}$. For the ATCA & Parkes HI, dense atomic clouds are distributed in the western shell. The HI clouds tend to be bright in the southwestern shell at $V_{\text{LSR}} = 245\text{--}255\text{ km s}^{-1}$, while the northwestern shell with the X-ray brightest rim is bright in HI at $V_{\text{LSR}} = 255\text{--}275\text{ km s}^{-1}$.

Figures 4(a), (b), and (c) are the position–velocity diagrams of $^{12}\text{CO}(J=1-0)$, $^{12}\text{CO}(J=3-2)$, and HI, whose integration ranges are shown as the dashed lines in Figure 1(d). We confirmed a cavity-like HI structure in a velocity range from 245 to 275 km s^{-1} in Figure 4(c), as previously mentioned by Paper I. In addition, we newly find a similar structure of CO, which is indicated by the dashed-black circle in Figures 4(a) and (b). The size of CO and HI cavity-like structures is roughly consistent with the diameter of 30 Dor C in decl.

3.4. Distribution of Proton Column Density

To derive the total proton column density $N_p(\text{H}_2+\text{HI})$ toward 30 Dor C, we used following equations:

$$N_p(\text{H}_2 + \text{HI}) = 2 \times N_p(\text{H}_2) + N_p(\text{HI})(\text{cm}^{-2}), \quad (3)$$

$$N_p(\text{HI}) = 1.823 \times 10^{18} \cdot W(\text{HI}) \cdot X(\text{cm}^{-2}), \quad (4)$$

where $N_p(\text{H}_2)$ is the proton column density of molecular form, $N_p(\text{HI})$ is the proton column density of atomic form, $W(\text{HI})$ is integrated intensity of HI, and X is a scaling factor. In general, $X = 1$ was used under the assumption of optically thin HI (e.g., Dickey & Lockman 1990). However, recent HI studies toward the high-latitude clouds indicate that the HI is not completely optically thin and $X \sim 1.5$ is better to trace the real amount of atomic hydrogen (Fukui et al. 2014, 2015; Okamoto et al. 2017; Hayashi et al. 2019a, 2019b). In the present study, we use $X = 1.7$ (see Appendix). Figures 5(a), (b), and (c) are maps of $N_p(\text{H}_2)$, $N_p(\text{HI})$, and $N_p(\text{H}_2+\text{HI})$, respectively. For the map of $N_p(\text{H}_2)$, four prominent structures corresponding to CO clouds A, D, H, and L are seen in the southwestern shell, which have a column density of $\sim 1.6 \times 10^{22}\text{ cm}^{-2}$ or higher. In the northwestern shell, there is a clumpy structure with a column density of $\sim 0.8 \times 10^{22}\text{ cm}^{-2}$. For the map of $N_p(\text{HI})$, the large column density of $\sim 0.6 \times 10^{22}\text{ cm}^{-2}$ is seen in the western shell, while the column density of the eastern shell is typically lower than $\sim 0.5 \times 10^{22}\text{ cm}^{-2}$. We also note that the highest value of $N_p(\text{HI}) \sim 1.0 \times 10^{22}\text{ cm}^{-2}$ is placed toward the X-ray brightest-rim. For the map of $N_p(\text{H}_2+\text{HI})$, the typical column density of the western shell is ~ 4 times higher than that of the eastern shell. In the western shell, the total proton column density is dramatically changed by region-to-region with $N_p(\text{H}_2+\text{HI}) \sim 0.3\text{--}5.4 \times 10^{22}\text{ cm}^{-2}$. In contrast, the eastern half of the shell is expected to show homogeneous gas distribution with $N_p(\text{H}_2+\text{HI}) \sim 0.4 \times 10^{22}\text{ cm}^{-2}$ with a small standard deviation of $\sim 0.1 \times 10^{22}\text{ cm}^{-2}$.

3.5. Detailed Comparison with the ISM and Synchrotron X-ray Properties

To test a physical connection between the ISM and X-ray properties, we compare the ISM distribution with the distributions of the photon index, absorbing column density, and synchrotron X-ray intensity presented by Babazaki et al. (2018). Their spatially resolved X-ray spectral analysis was carried out with a scale of $\sim 10\text{ pc}$.

Figure 6 shows a spatial comparison between X-ray properties and ISM. The maps of the photon index, X-ray absorbing column density $N_{\text{H},X}$, absorption-corrected flux of synchrotron X-rays that we used were derived and published by Babazaki et al. (2018). These contours indicate $N_p(\text{H}_2+\text{HI})$. Figure 6(a) represents the photon index map. We note that the regions with small photon indices < 2.4 are seen toward the western shell with the dense ISM, while the eastern shell has no dense ISM and smaller photon indices. Figure 6(b) indicates $N_{\text{H},X}$. In the northwestern shell, the ISM shows a good spatial correspondence with $N_{\text{H},X}$. However, low $N_{\text{H},X}$ of $\sim 0.5 \times 10^{22}\text{ cm}^{-2}$ is found in the southwestern region, which is indicated by the blue box in Figure 6(b), despite the ISM-rich environment around the position of $(\alpha_{\text{J2000}}, \delta_{\text{J2000}}) \sim (5^{\text{h}} 35^{\text{m}} 45^{\text{s}}0, -69^{\circ} 13^{\text{m}} 12^{\text{s}})$. Figure 6(c) shows the absorption-

Table 3
Physical Properties of $^{12}\text{CO}(J=1-0)$ Clouds

Name	$\alpha(2000)$ (h m s)	$\delta(2000)$ ($^{\circ}$ ' ")	T_R^* (K)	V_{peak} (km s^{-1})	ΔV (km s^{-1})	Size (pc)	M_X ($10^3 M_{\odot}$)	n_{H_2} (10^2 cm^{-3})
(1)	(2)	(3)	(4)	(5)	(6)	(7)	(8)	(9)
A1	5:35:24.3	-69:11:56.3	4.3	249.7	3.5	9.9	4.0	3.2
A2	5:35:25.1	-69:12:02.3	7.5	255.2	3.7	12.0	8.0	3.6
B	5:35:26.2	-69:11:28.3	1.8	251.6	1.9	5.9	0.6	2.2
C	5:35:32.6	-69:11:20.3	2.5	250.3	2.1	7.8	1.1	1.9
D1	5:35:36.3	-69:12:22.3	6.3	251.2	4.3	13.1	10.7	3.7
D2	5:35:36.0	-69:12:18.3	5.5	255.9	2.4	11.2	4.8	2.6
E	5:35:37.5	-69:12:56.3	1.9	248.4	3.6	7.3	1.5	3.0
F	5:35:43.5	-69:10:38.4	1.6	268.4	3.1	9.8	1.9	1.6
G1	5:35:43.5	-69:09:36.4	2.5	269.3	1.9	12.1	2.7	1.2
G2	5:35:42.0	-69:09:52.3	2.4	269.9	1.7	12.1	2.7	1.2
H	5:35:45.3	-69:13:12.4	4.3	258.0	5.9	12.8	10.7	4.0
I	5:35:46.9	-69:09:06.4	3.1	269.1	2.2	12.9	4.6	1.6
J	5:35:50.6	-69:10:32.4	4.1	248.2	3.3	8.9	1.9	2.1
K	5:35:50.6	-69:13:12.4	2.4	247.6	4.0	11.0	4.0	2.3
L	5:35:52.5	-69:12:42.4	4.7	247.3	4.7	11.0	6.7	3.9
M	5:35:51.4	-69:11:28.4	1.8	271.3	3.0	9.2	1.9	1.9
N1	5:35:52.1	-69:09:52.4	2.1	266.6	1.9	7.7	1.0	1.7
N2	5:35:53.6	-69:09:56.4	1.6	270.7	1.6	9.5	1.0	0.9
O	5:35:54.7	-69:14:28.4	3.0	257.2	1.5	6.5	0.8	2.3
P	5:36:00.4	-69:13:32.3	2.8	254.8	2.9	7.9	1.8	2.9
Q	5:35:58.1	-69:10:32.4	2.4	273.4	1.9	11.1	2.2	1.2
R	5:36:01.1	-69:11:14.3	1.8	273.1	2.3	12.5	3.8	1.5
S	5:36:05.6	-69:13:22.3	2.4	252.8	3.5	9.4	3.0	2.8

Note. Col. (1): Cloud name. Cols. (2–3): Position of the maximum CO intensity for each velocity component. Cols. (4–6): Physical properties of the $^{12}\text{CO}(J=1-0)$ emission obtained at each position. Col. (4): Peak radiation temperature, T_R^* . Col. (5): V_{peak} derived from a single Gaussian fitting. Col. (6): Full-width at half-maximum (FWHM) line width, ΔV . Col. (7): Cloud size defined as $(A/\pi)^{0.5} \times 2$, where A is the total cloud surface area surrounded by the contour of 5σ level of signal over noise ratio (see the text). Col. (8): Mass of the cloud which was derived by using the relationship between the molecular hydrogen column density $N(\text{H}_2)$ and the $^{12}\text{CO}(J=1-0)$ intensity $W(^{12}\text{CO})$, $N(\text{H}_2) = 7.0 \times 10^{20} [W(^{12}\text{CO})/(\text{K km s}^{-1})]$ (Fukui et al. 2008). Col. (9): The density of hydrogen molecules.

corrected synchrotron X-ray intensity map. The X-ray intensity is greater than $\sim 1 \times 10^{-7} \text{ erg s}^{-1} \text{ cm}^{-2} \text{ sr}^{-1}$ toward the eastern shell, where the ISM is rich. The X-ray intensity is increased around the ISM peaks (e.g., clouds C, D1, D2, N1, and N2). Meanwhile, the northeastern shell is also bright in the synchrotron X-rays, where the ISM column density is low. Figure 6(d) is the average hard X-ray counts, which is the same data with images of Figures 1(b) and (c), for each pixel the same as Figures 6(a)–(c). The X-ray counts in the western side of the shell tend to be larger than that on the eastern side.

Figure 7 indicates correlation plots between the X-ray properties and $N_p(\text{H}_2+\text{HI})$. Figure 7(a) shows a correlation plot between the photon index and $N_p(\text{H}_2+\text{HI})$. The photon index tends to be small where the column density is high. A negative correlation between the photon index and column density is seen. The correlation coefficient is about -0.57 for $N_p(\text{H}_2+\text{HI})$. Figure 7(b) shows a scatter plot between the absorbing column density and $N_p(\text{H}_2+\text{HI})$. The absorbing column density is generally proportional to $N_p(\text{H}_2+\text{HI})$, except for the three points within the ranges of $N_p(\text{H}_2+\text{HI}) \sim (1.4-1.7) \times 10^{22} \text{ cm}^{-2}$ and the absorbing column density of $\sim 0.5 \times 10^{22} \text{ cm}^{-2}$. The correlation coefficient is estimated to be ~ 0.46 . Figure 7(c) shows a correlation plot between the X-ray intensity and $N_p(\text{H}_2+\text{HI})$ in double logarithm. We can see that there is a weak positive correlation between the two. We derived the correlation coefficient to be ~ 0.45 .

4. Discussion

4.1. Interstellar Gas Motion

Paper I found an HI cavity-like structure in the velocity range from 251 to 276 km s^{-1} by using ATCA & Parkes HI data with $1'$ resolution. The authors showed that the momentum of these interstellar gas is 10 times larger than that of stellar winds. Therefore, Paper I suggested that the lack of the momentum might be derived from pre-existing gas motion. In this section, we re-examine the origin of the interstellar gas motion using the new HI data with $16''$ resolution and ALMA $^{12}\text{CO}(J=1-0)$ data.

In Figures 4(a) and (b), we find two CO components at $V_{\text{LSR}} = 245-265 \text{ km s}^{-1}$ and $V_{\text{LSR}} = 265-275 \text{ km s}^{-1}$, which show the cavity-like structure. We also find a similar structure of HI in Figure 4(c), which is consistent with the results by Paper I. Because the decl. extents of CO and HI cavity-like structures are roughly consistent with the diameter of X-ray shell, it is natural to think that the cavity-like structures are related to be previous stellar activities of 30 Dor C: such as strong stellar winds from high-mass stars and clusters, and/or past supernova explosions. In the present paper, the velocity range of the structure was determined as $\sim 30 \text{ km s}^{-1}$ taking into account the cavity-like structure of not only HI but also CO into account, which is different from the velocity range mentioned in Paper I. This difference could arise from the velocity dispersion of $\sim 10 \text{ km s}^{-1}$ of each component. Therefore, in the present study we assumed that molecular and

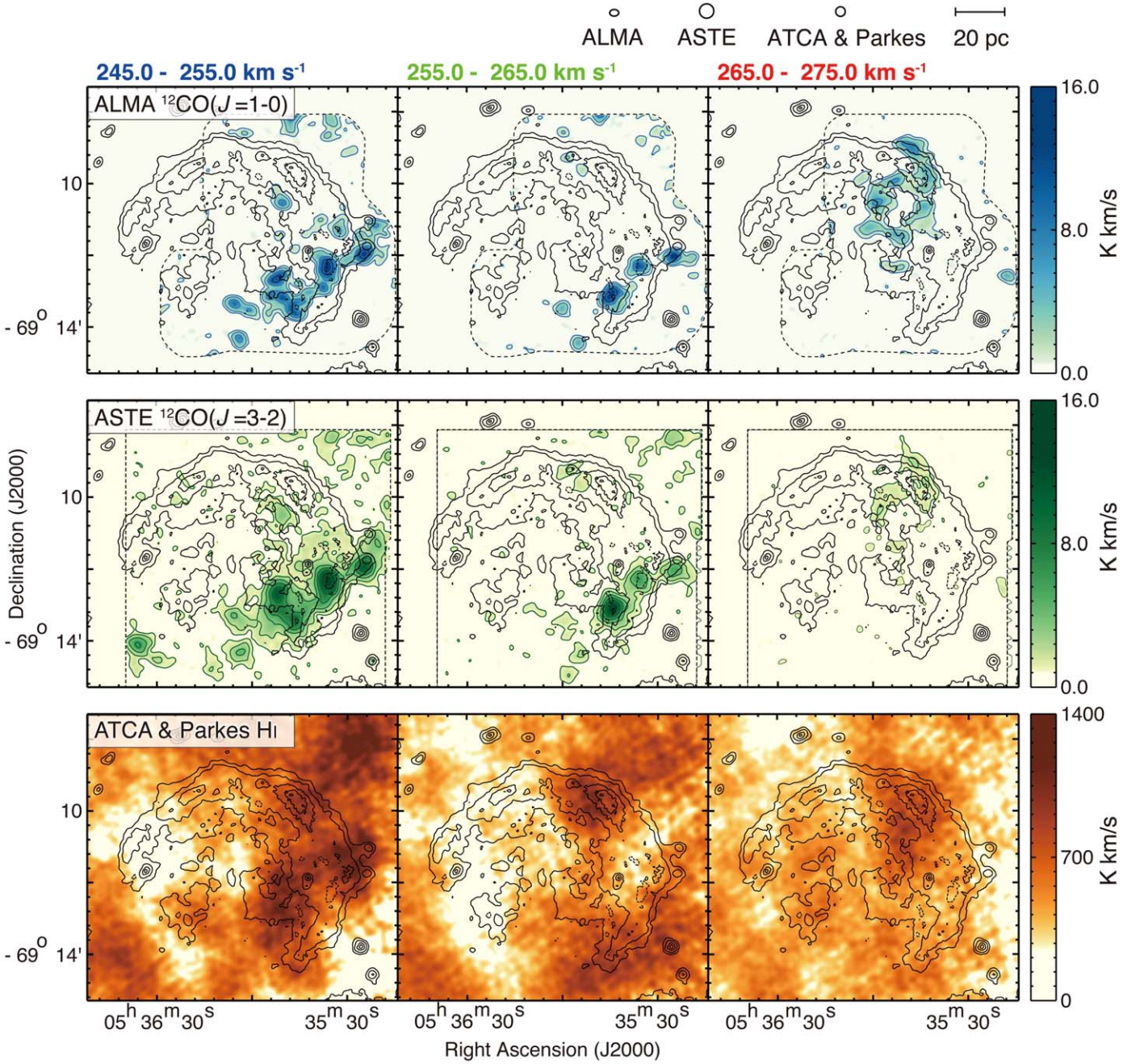


Figure 3. Velocity channel maps of ALMA $^{12}\text{CO}(J=1-0)$ (top panels), ASTE $^{12}\text{CO}(J=3-2)$ (middle panels), and ATCA & Parkes HI (bottom panels) overlaid with the same X-ray contours as Figure 1(d). Each panel shows the CO and HI intensity maps integrated over the velocity range from 245.0 to 275.0 km s^{-1} every 10.0 km s^{-1} . The contour levels are 0.74, 1.92, 5.46, 11.4, and 19.6 K km s^{-1} for $^{12}\text{CO}(J=1-0)$; 0.95, 1.90, 3.63, 5.87, 8.53, 11.5, and 14.9 K km s^{-1} for $^{12}\text{CO}(J=3-2)$.

atomic gas share the same motion in a velocity range of $\sim 30 \text{ km s}^{-1}$.

First, we consider the momentum of the associated gas motion. Assuming that the CO/HI cavity-like structure shares the expanding gas motion, the expansion velocity is $\sim 15 \text{ km s}^{-1}$. The total mass of the interstellar gas associated with 30 Dor C is estimated to be $\sim 3.6 \times 10^5 M_{\odot}$, the mass of the molecular gas is $\sim 1.2 \times 10^5 M_{\odot}$, and that of atomic gas is $\sim 2.4 \times 10^5 M_{\odot}$. Consequently, the momentum of the expanding gas motion associated with the superbubble is calculated to be $\sim 5.3 \times 10^6 M_{\odot} \text{ km s}^{-1}$. Meanwhile, the total momentum of

the stellar winds is $\sim 2.3 \times 10^5 M_{\odot} \text{ km s}^{-1}$ from the 26 O-type stars and six WR stars (Bonanos et al. 2009).

Here the momentum of the stellar wind D_{mom} is calculated to be $D_{\text{mom}} = m_{\text{loss}} \times v \times t$, where m_{loss} is the mass loss rate, v is the wind velocity, and t is the wind duration time. The typical wind momentum of high-mass star could be calculated by considering $m_{\text{loss}} \sim 1 \times 10^{-6} M_{\odot} \text{ yr}^{-1}$, $v \sim 2000 \text{ km s}^{-1}$, and $t \sim 10^6 \text{ yr}$ for an O-type star; and $m_{\text{loss}} \sim 3 \times 10^{-5} M_{\odot} \text{ yr}^{-1}$, $v \sim 2500 \text{ km s}^{-1}$, and $t \sim 3 \times 10^5 \text{ yr}$ for a WR star (see Abbott 1982).

Because stellar winds inject momentum into interstellar gas at $\sim 20\%$ efficiency (Weaver et al. 1977), the effective

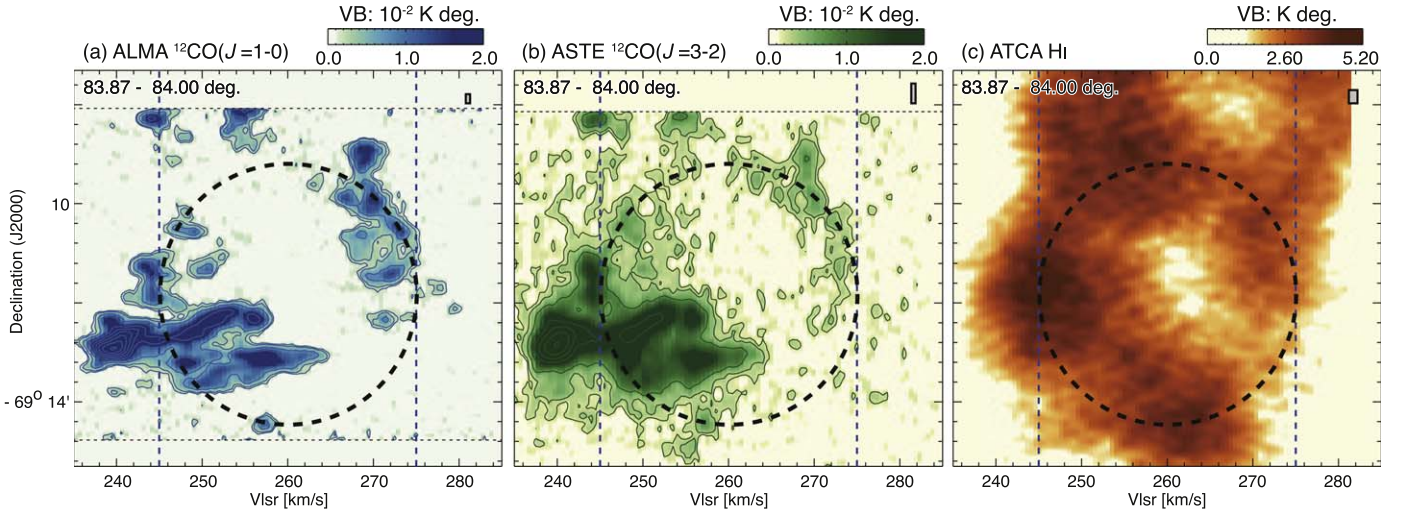


Figure 4. Position-velocity diagrams of the (a) ALMA $^{12}\text{CO}(J=1-0)$, (b) ASTE $^{12}\text{CO}(J=3-2)$, and (c) ATCA & Parkes HI. The integration ranges are from $83^{\circ}87'$ to $84^{\circ}00'$ in the R.A., as shown in Figure 1(d) by the dashed-blue lines. The contour levels are 0.25 ($\sim 5\sigma$), 0.40, 0.85, 1.60, 2.65, 4.00, 5.65, 7.60, 9.85, and 12.4×10^{-2} K deg for $^{12}\text{CO}(J=1-0)$; 0.26 ($\sim 8\sigma$), 0.42, 0.88, 1.66, 2.76, 4.16, 5.88, and 7.90×10^{-2} K deg for $^{12}\text{CO}(J=3-2)$. The resolutions are indicated in the top right-hand corner of each figure. All of the black-dashed circles are same size and show the shell-like shell toward 30 Dor C.

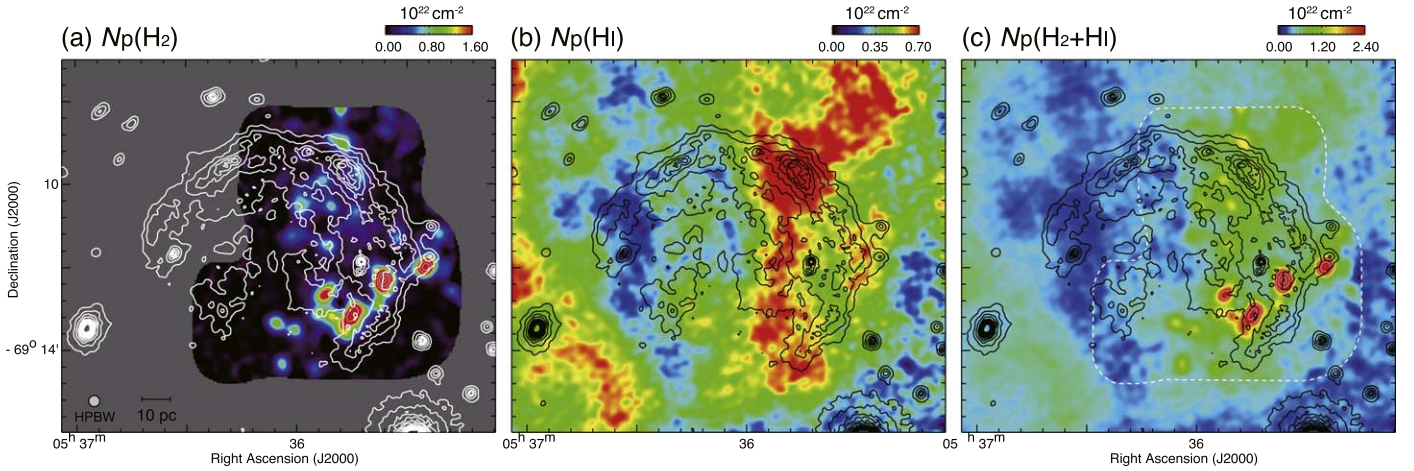


Figure 5. Maps of (a) $N_p(\text{H}_2)$, (b) $N_p(\text{HI})$, and (c) $N_p(\text{H}_2+\text{HI})$. The velocity range is from $V_{\text{LSR}} = 245$ to 275 km s^{-1} . White and black contours are hard-band XMM-Newton X-rays delineated 5.00, 10.0, 19.1, 31.0, 45.0, 60.9, and $78.5 \text{ counts s}^{-1} \text{ deg}^{-2}$. The white-dashed line indicates the observed area of $^{12}\text{CO}(J=1-0)$ line emission.

momentum by stellar winds into associated gas is $\sim 4.6 \times 10^4 M_{\odot} \text{ km s}^{-1}$, which is only $\sim 1\%$ of the momentum of the expanding gas motion.

The gas distribution of the line-of-sight also implies the existence of other mechanisms responsible for the formation of the cavity-like structure. Figure 6(b) represents the spatial relation between the X-ray absorbing column density and the total proton column density $N_p(\text{H}_2+\text{HI})$. Figure 7(b) shows that the absorbing column density is roughly proportional to $N_p(\text{H}_2+\text{HI})$ in many regions. However, in the data points of the southwestern region which plotted as open circles, absorbing column density is small compared $N_p(\text{H}_2+\text{HI})$. Therefore, we interpret from this relation that in the southwestern region, the interstellar gas has not contributed to the absorption of X-rays; in other words, the gas is located behind 30 Dor C. Figure 8 represents the relationships between the absorbing column density and $N_p(\text{H}_2+\text{HI})$ for (a) the blue-shifted gas ($V_{\text{LSR}} = 245$ – 260 km s^{-1}), and for (b) the red-shifted gas ($V_{\text{LSR}} = 260$ – 275 km s^{-1}). Figure 8(a) shows that the blue-shifted gas is dominant in the southwestern region, and thus the

blue-shifted gas is expected to be located behind 30 Dor C. Meanwhile, Figure 8(b) shows that the red-shifted gas is located in the region where the absorbing column density is roughly proportional to $N_p(\text{H}_2+\text{HI})$. Thus, the red-shifted gas is expected to be located in front of 30 Dor C. In the formation of a cavity-like structure by expanding motion, it is generally thought that the blue-shifted gas is located in front of the red-shifted gas. In contrast, the blue-shifted gas is located behind the red-shifted gas. This kinematic signature could arise with infall and a collapsing, rather than expanding shell. Therefore, it is considered that other mechanisms are responsible for the formation of the gas structure whose velocity difference is $\sim 30 \text{ km s}^{-1}$.

We suggest that the gas structure, large velocity separation of 30 km s^{-1} and unusual kinematic structure are driven by a galaxy-scale interstellar gas structure, as mentioned by Paper I. In the LMC, it has been known that there are two HI velocity components whose velocity difference is 50 km s^{-1} (e.g., Luks & Rohlfs 1992). Fujimoto & Noguchi (1990) proposed a scenario in which the last tidal interaction between the LMC

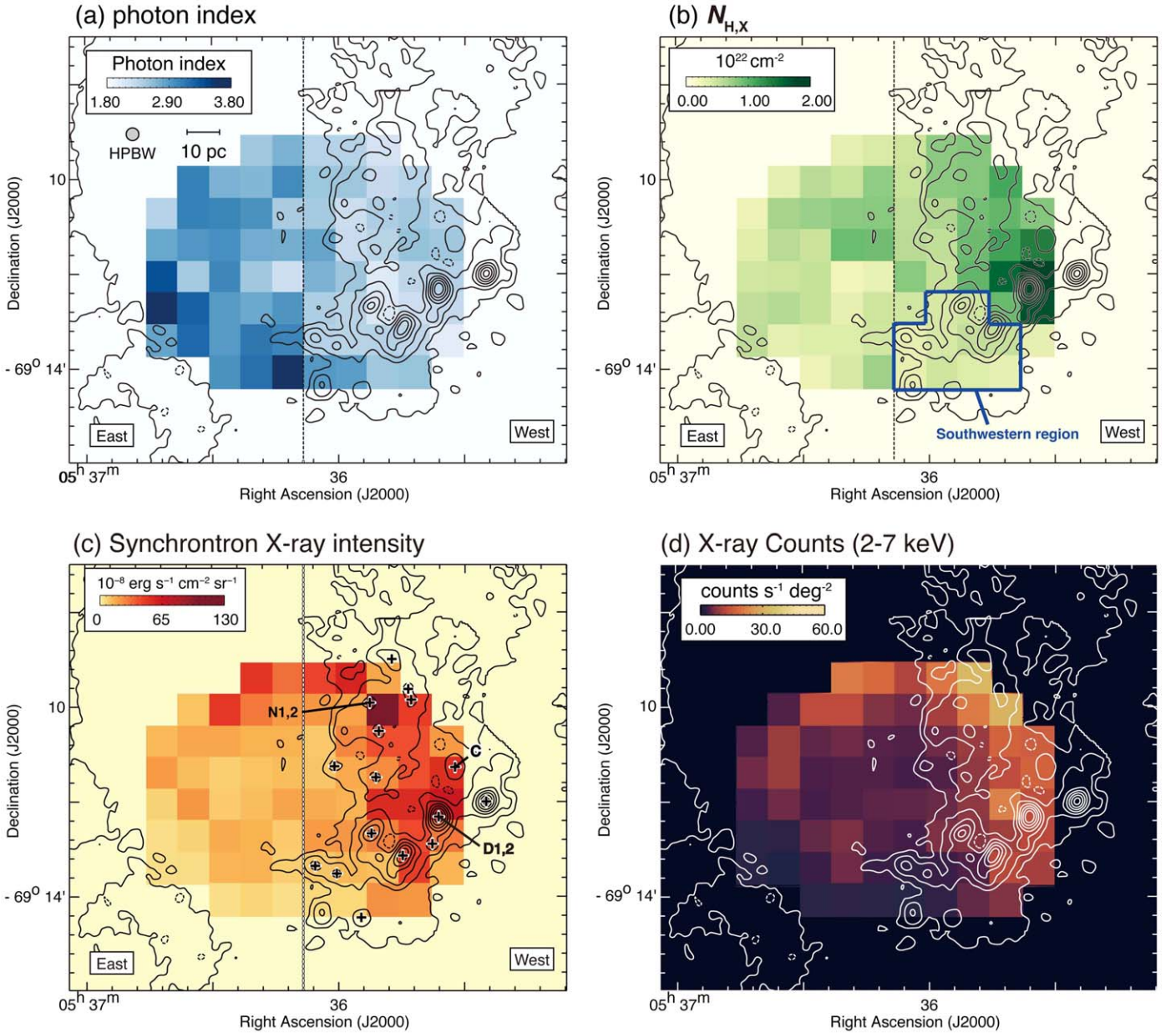


Figure 6. Maps of (a) the X-ray photon index, (b) the absorbing column density $N_{H,X}$, (c) the absorption-corrected synchrotron X-ray intensity, and (d) the average hard X-ray counts; which is the same data as images of Figures 1(b) and (b). Contours indicate $N_p(H_2+HI)$ and the contour levels are 0.53, 0.79, 1.27, 2.61, 3.44, 4.35, and $5.35 \times 10^{22} \text{ cm}^{-2}$.

and Small Magellanic Cloud occurring 0.2 Gyr ago perturbed the gas in the both galaxies and then formed two velocity components. This galaxy interaction scenario has been supported by numerical simulation by Bekki & Chiba (2007). Fukui et al. (2017) presented the spatial and velocity distribution of these HI components in the high-mass star-forming region R136 in the eastern side of the LMC. They discovered the bridge feature and complementary distribution between the two HI components that caused the high-mass star formation triggered by a cloud-cloud collision, such as in the Galactic molecular clouds (e.g., Fukui et al. 2018). Therefore, two HI components were interpreted as interacting with each other around R136. Fukui et al. (2017) concluded that the interaction with two HI components triggered the high-mass star formation in and around R136. Likewise, in the star-forming region N44 in the LMC, Tsuge et al. (2019) presented

a scenario of the high-mass star formation triggered by the interaction of the HI components. In 30 Dor C, Figure 8 presents that high-mass stars are located around the interstellar gas peaks. In addition, it is considered that the blue-shifted gas approaching from behind the superbubble 30 Dor C is not involved in the past high-mass star formations because high-mass stars are not distributed in the southwestern region. However, the current resolution is not good enough for a further detailed study of star formation in 30 Dor C. The high-mass star formation will be studied in more detail using ALMA 12 m CO data with higher resolution ($\sim 3''$).

Figure 9(a) shows the large-scale integrated intensity map of HI around R136 containing 30 Dor C, which is indicated by a green-dashed circle, and Figure 9(b) shows the position-velocity diagram. As noted in Figure 9(b), there are two HI velocity components, which are indicated by red- or blue-

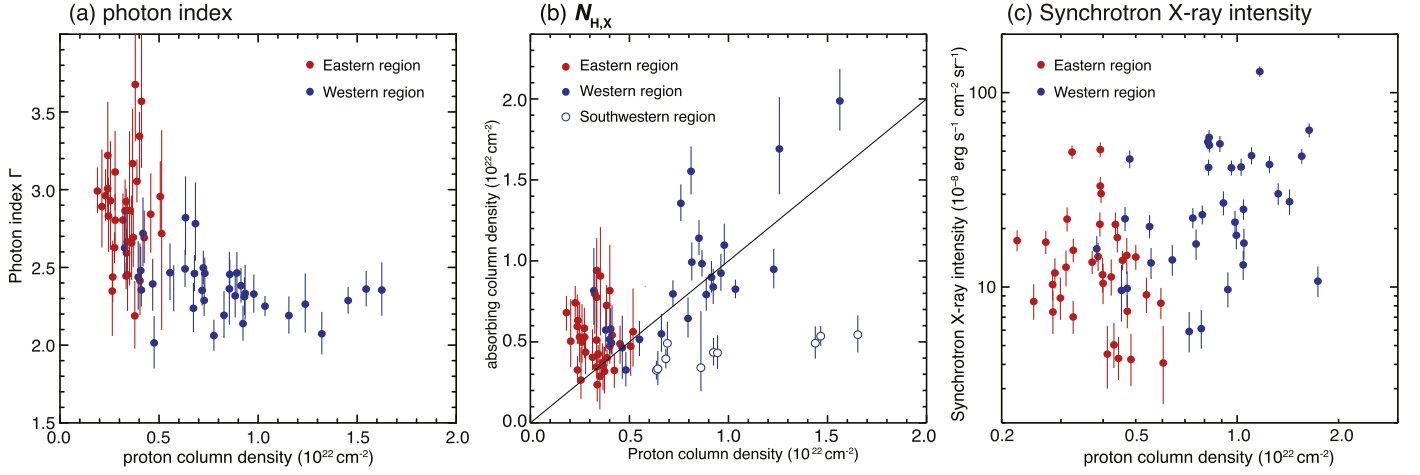


Figure 7. Correlation plots for (a) the photon index vs. $N_p(\text{H}_2+\text{HI})$, (b) $N_{\text{H,X}}$ vs. $N_p(\text{H}_2+\text{HI})$, and, (c) the absorption-corrected synchrotron X-ray intensity and $N_p(\text{H}_2+\text{HI})$. Eastern and western regions are defined as in Figure 6. (b) Open circles represent the data that were extracted from the southwestern region that is enclosed by a blue line in Figure 6(b). The black line shows the proportional relation.

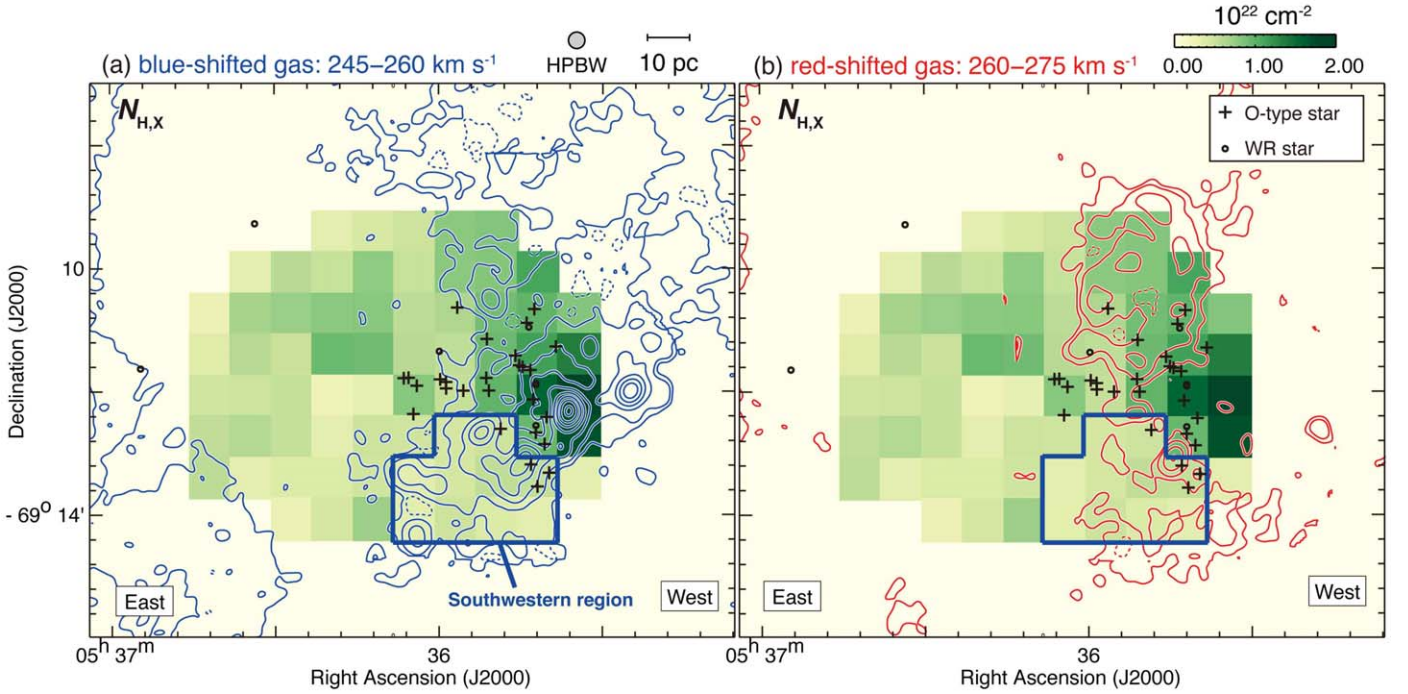


Figure 8. Maps of $N_{\text{H,X}}$ superposed on the contours of total proton column density for the (a) blue-shifted gas, and for the (b) red-shifted gas. The velocity range of the blue-shifted gas is 245–260 km s⁻¹, and that of the red-shifted gas is 260–275 km s⁻¹. The contour levels are 0.292, 0.414, 0.780, 1.39, 2.24, 3.34, 4.68 $\times 10^{22} \text{ cm}^{-2}$. The black crosses and circles indicate positions of O-type stars and WR stars, respectively.

dashed lines with the velocity difference $\sim 50 \text{ km s}^{-1}$. The velocity difference in the western side is smaller than that on the eastern side. Around 30 Dor C, two velocity components seem to merge and the velocity difference becomes $\sim 30 \text{ km s}^{-1}$. This is in agreement with the velocity difference of the CO/HI cavity-like structure in 30 Dor C (see Figure 4). In Figure 9(c), the velocity ranges of the blue- and red-shifted gas shown in Figure 8 are indicated as red and blue straps, respectively. These two associated gases with 30 Dor C roughly correspond to the two large-scale components that are indicated by red- and blue-dashed lines. The associated gas structure is thought to be related to the large-scale gas structure. This HI gas structure suggests the possibility that high-mass star formation is triggered by the HI colliding flow in

30 Dor C, which is the same as R136 and N44 (Fukui et al. 2017; Tsuge et al. 2019). In this case, it is likely that coeval high-mass star formation was caused and that multiple supernovae exploded in 30 Dor C.

The pre-existing gas motion can also explain the relative positions of the red- and blue-shifted clouds, which are opposite of what is expected in the expanding motion. Sano et al. (2015) reported a similar trend that the red-shifted CO clouds produced by expanding motion are located on the far side of the Galactic SNR RX J1713.7–3946. The authors discussed that the relative position of the CO clouds is explicable if the pre-existent gas motion caused by overlapping CO supershell GS 347 + 0.0–21 is dominant for the CO clouds instead of expansion. In 30 Dor C, the pre-existing gas

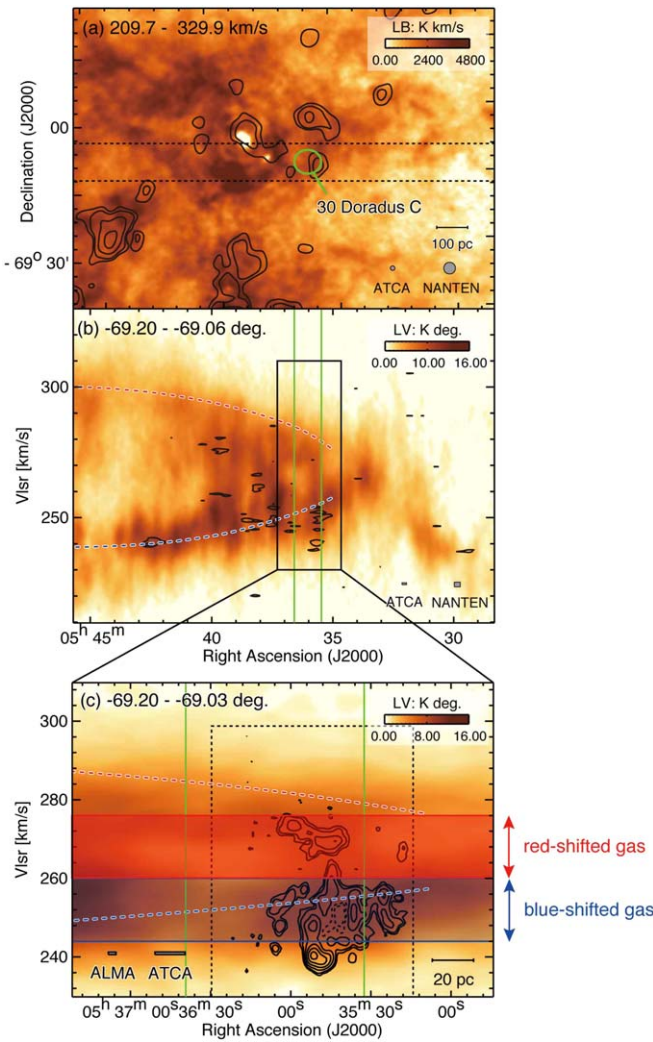


Figure 9. (a) Integrated intensity map of HI (image) and $^{12}\text{CO}(J=1-0)$ (contours) with the integration velocity range of $V_{\text{LSR}} = 209.7\text{--}329.9\text{ km s}^{-1}$. The green circle illustrates the 30 Dor C and the black-dashed lines indicate the integration range of (b). The contour levels are $0.859\ (5\sigma)$, 1.72 , 4.30 , and 8.59 K km s^{-1} . (b) Position–velocity diagram of HI (image) and $^{12}\text{CO}(J=1-0)$ (contours). The position of 30 Dor C is indicated by the green lines. The integration ranges in decl. are from $-69^\circ20'$ to $-69^\circ03'$. The contour levels are 0.84 , and $1.31 \times 10^{-2}\text{ K km s}^{-1}$. (c) Position–velocity diagram of HI and $^{12}\text{CO}(J=1-0)$ that enlarges the square region from (b). The red-shifted and blue-shifted gas correspond to Figures 8(a) and (b). The contour levels are 0.35 , 0.70 , 1.75 , 3.50 , 5.95 , and $9.10 \times 10^{-2}\text{ K km s}^{-1}$.

motion was driven by HI colliding flow and the pre-existing gas motion is likely dominant for the expanding gas motion, due to the stellar feedback by associated high-mass stars. Note that the spatial scale of the colliding flow is $\sim 1^\circ$, while that of the expanding gas motion is $\sim 6'$. Therefore, the two kinematic motions are independent but complicated toward 30 Dor C. Investigating the gas structure around 30 Dor C using high-resolution Australian Square Kilometre Array Pathfinder (ASKAP) HI data can better characterize the mechanism responsible for the structure formation.

4.2. Origin of the Synchrotron X-ray

30 Dor C is unique among superbubbles because it has a bright synchrotron X-ray shell. It is known that the maximum energy of accelerated particle in 30 Dor C is higher than that in the single SNRs (e.g., Bamba et al. 2004; Yamaguchi et al.

2009). Consequently, it is important to explore 30 Dor C to improve our understanding of cosmic-ray acceleration in superbubbles. Sano et al. (2017) focused the distribution of interstellar gas in the northwestern shell and argued that magnetic turbulence is effectively amplified by shock-cloud interaction. Meanwhile, Bamba (2004) and Kavanagh et al. (2019) argued that magnetic field strength is lower than $20\ \mu\text{G}$. Kavanagh et al. (2019) suggested that, except in the northwestern shell, bright synchrotron X-ray is derived from high-energy electrons that are accelerated in the shock front. Based on the size of superbubbles to which the dynamical age corresponds, Babazaki et al. (2018) suggested that 30 Dor C is on a phase of high-energy particle acceleration and thus synchrotron X-rays are bright. In this section, we argue that the bright synchrotron X-ray emission is derived from the amplification of the magnetic field at the downstream of the shock front by shock-cloud interaction in the western shell with the rich interstellar gas.

First, based on large-scale (10 pc scale) distributions of interstellar gas and synchrotron X-rays, we argue that interstellar gas is physically related to synchrotron X-rays. Both molecular and atomic clouds tend to be distributed at the western side of the shell where synchrotron X-rays are bright (see Figures 1(b)–(d)). In addition, $N_p(\text{H}_2+\text{HI})$ in the western side of the shell is $\sim 2\text{--}3$ times higher than that in the eastern side (see Figure 5). Consequently, we consider that some mechanisms are responsible for an increase of the synchrotron X-ray intensity in such cloud-rich regions. This physical relation seems to have appeared quantitatively as the positive correlation between the proton column density and the absorption-corrected synchrotron X-ray intensity (see Figure 6(b), correlation coefficient ~ 0.40).

Next, based on small-scale (a few pc scale) distributions of CO clouds and synchrotron X-rays, we argue that the relation of the two may be driven by shock-cloud interaction. As shown in Figure 1(b), it is found that all bright synchrotron X-ray spots are associated with CO clouds (Clouds A1, A2, B, C, D1, D2, E, F, G1, G2, I, J, L, N1, and N2) in the western shell, and the separations between each peak are a few pc. These results are considered to be due to the SN shock interacting with the interstellar gas, which then amplifies the synchrotron X-ray by intensifying a magnetic field around the shocked gas. In fact, these relationships between the interstellar gas and X-rays were observed in the Galactic single SNRs (e.g., RX J1713.7–3946, and RCW 86). The result was interpreted as the turbulence amplification of magnetic field up to mG around the dense cloud cores (e.g., Sano et al. 2015, 2017). Interestingly, the typical separation between the peaks of interstellar gas and X-rays in 30 Dor C is larger than the average separations in the Galactic SNRs, which are $1.2 \pm 0.6\text{ pc}$ for RX J1713.7–3946, and $1.8 \pm 1.3\text{ pc}$ for RCW 86. Therefore, it is likely that there is a smaller structure in 30 Dor C, which is the same as that in Galactic SNRs. It is expected that a more detailed structure will be revealed by using the new ALMA 12 m array data with high-resolution.

Although the strong magnetic field is expected under the shock-cloud interaction scenario in 30 Dor C, Kavanagh et al. (2019) claimed low magnetic field strength. The authors made radial profiles of X-rays in the synchrotron shell in the northwest (NW), southwest, and northeast, and made model fitting for filamentary X-rays. They found that the post-shock magnetic field strength is less than $20\ \mu\text{G}$. In their analysis,

they adopted a width greater than 10 pc in the azimuthal direction. The width is 20 times larger than that of the typical filamentary distribution (Bamba et al. 2005), which makes it impossible to resolve the enhanced magnetic field of sub-pc scale (e.g., see RXJ1713, Sano et al. 2010, 2013). Additionally, the scale of the width is two orders larger than the scale of magnetic field amplification that we consider (Uchiyama et al. 2007; Inoue et al. 2009). The authors noted that the fitting was not successful in the regions of molecular gas (sectors 6 and 7 in the NW). The argument that the shock-cloud interaction does not affect the magnetic field and X-rays in the LMC (Kavanagh et al. 2019) is therefore not justified, and measurements of the magnetic field in 30 Dor C require careful re-examination.

4.3. Efficient Acceleration of Cosmic-ray Electrons

Babazaki et al. (2018) presented the spatial variation of the photon index between eastern and western parts of the shell in 30 Dor C. The authors mainly found two observational trends: (1) small photon indices are seen in the western part where dense molecular clouds are associated, and (2) absorption-corrected synchrotron X-ray intensity shows a negative correlation with the photon indices. The authors concluded that these trends could be understood as magnetic field amplification around the shocked clouds via shock-cloud interaction (e.g., Inoue et al. 2009, 2012; Sano et al. 2010, 2013). However, a detailed spatial comparison between interacting clouds and X-ray properties has never been presented. In this section, we discuss the effective cosmic-ray acceleration and the amplified turbulence in 30 Dor C based on the spatial distributions of the interstellar gas and the photon index.

We argue that cosmic-ray electrons are accelerated effectively at least a few TeV at the region where the photon index is small (<2.4), as presented by Babazaki et al. (2018). In the regime of Bohm diffusion, the energy flux of synchrotron X-rays from accelerated electrons has cut-off power-law distributions through the classical diffusive shock acceleration mechanism. It is considered that a small (large) photon index of synchrotron X-rays corresponds to a high (low) maximum energy of accelerated electrons (roll-off energy) when the energy distribution is fitted by the single power-law model. This is a useful interpretation if there is a lack of photon statistics; in other words, when the energy distribution cannot be fitted by cut-off power-law model. Based on the same interpretation, Sano et al. (2015) presented the spots where high-energy electrons are accelerated. They divided the Galactic SNR RX J1713.7–3946 into more than 300 regions and performed the same analysis as Babazaki et al. (2018).

The roll-off energy of synchrotron X-ray from accelerated electron in the regime of Bohm diffusion is described as follows (Zirakashvili & Aharonian 2007)

$$\varepsilon_0 = 0.55 \times \left(\frac{v_{\text{sh}}}{3000 \text{ km s}^{-1}} \right)^2 \eta^{-1} \text{ (keV)}. \quad (5)$$

Here v_{sh} is the shock speed. η (>1) is a gyro factor, which represents the degree of turbulence in the upstream. In the Bohm limit, η is close to 1 due to a strong magnetic turbulence. As can be seen from Equation (5), the roll-off energy depends on the shock speed and the turbulence in the upstream of the shock. Hereafter, we examine the effect of both the shock velocity and gyro factor.

4.3.1. Case 1: Shock Velocity Variation

We discuss the effects of SN explosions to evaluate the variation of shock speed v_{sh} in Equation (5). First, we predict that the center of the last SN explosion would be in the western side of the shell because high-mass stars are found to be located in the western shell. In this case, the shock velocity of the explosion center (or the western half of the shell) is faster than that of the eastern half of 30 Dor C; and thus, a large roll-off energy (or small photon index) is expected in the western shell according to Equation (5). To confirm this relationship more quantitatively, we plotted east–west radial profiles of photon indices centered on the center of mass of the high-mass star cluster; as shown in Figures 10(a) and (b). These profiles show that photon indices tend to be small near the center of the high-mass star cluster. In addition, these results suggest that single or multiple SNe have occurred in the high-mass star cluster, which accelerated cosmic-ray electrons via diffusive shock acceleration.

4.3.2. Case 2: Shock-cloud Interaction Induced Variation of the Gyro Factor

We also argue that the shock-cloud interaction may affect the spatial variation of photon indices. Figures 10(c) and (d) indicate the eastern and western radial profiles of $N_p(\text{H}_2+\text{HI})$. We found that $N_p(\text{H}_2+\text{HI})$ is small in the region where the photon index is large (Figure 10). This is the same trend as the results in Figures 6(a) and 7(a). If this relationship is true, then it is considered that the roll-off energy is extended by strong magnetic turbulence (i.e., η in Equation (5) is close to 1) around the interstellar gas, due to the shock-cloud interactions mentioned in Section 4.2. However, the relationship between the photon index and the interstellar gas is unclear at this time because spatial resolution of photon index is $\sim 10 \times 10$ pc, which is not enough to reveal the connection. We expect that the relationship will be understood by a deep Chandra observation, which will be able to show a more detailed spatial variation of distribution of the photon index in 30 Dor C.

5. Summary

We carried out new high-resolution study of the interstellar medium toward the LMC superbubble 30 Dor C. We explored the role of the interaction between the shock of an expanding bubble and the interstellar medium, and we examined its role in the high-energy radiation; in particular, non-thermal X-rays. The main conclusions of the study are summarized as follows;

1. The new high-resolution of ALMA and ASTE has allowed us to reveal detailed distributions of the 23 CO clouds with radius of $\sim 3\text{--}6$ pc. A comparison of the CO distribution with the non-thermal X-rays of XMM–Newton has revealed enhanced X-rays around the CO clouds. This is due to the shock-cloud interaction, which was numerically simulated by MHD (Inoue et al. 2012).
2. The total column density of the interstellar protons in atomic and molecular form are compared with the X-ray photon index. We see a trend for the photon index to become smaller toward higher column density, while scattering is large. This is also consistent with the shock-cloud interaction, which produces higher energy cosmic-ray electrons.

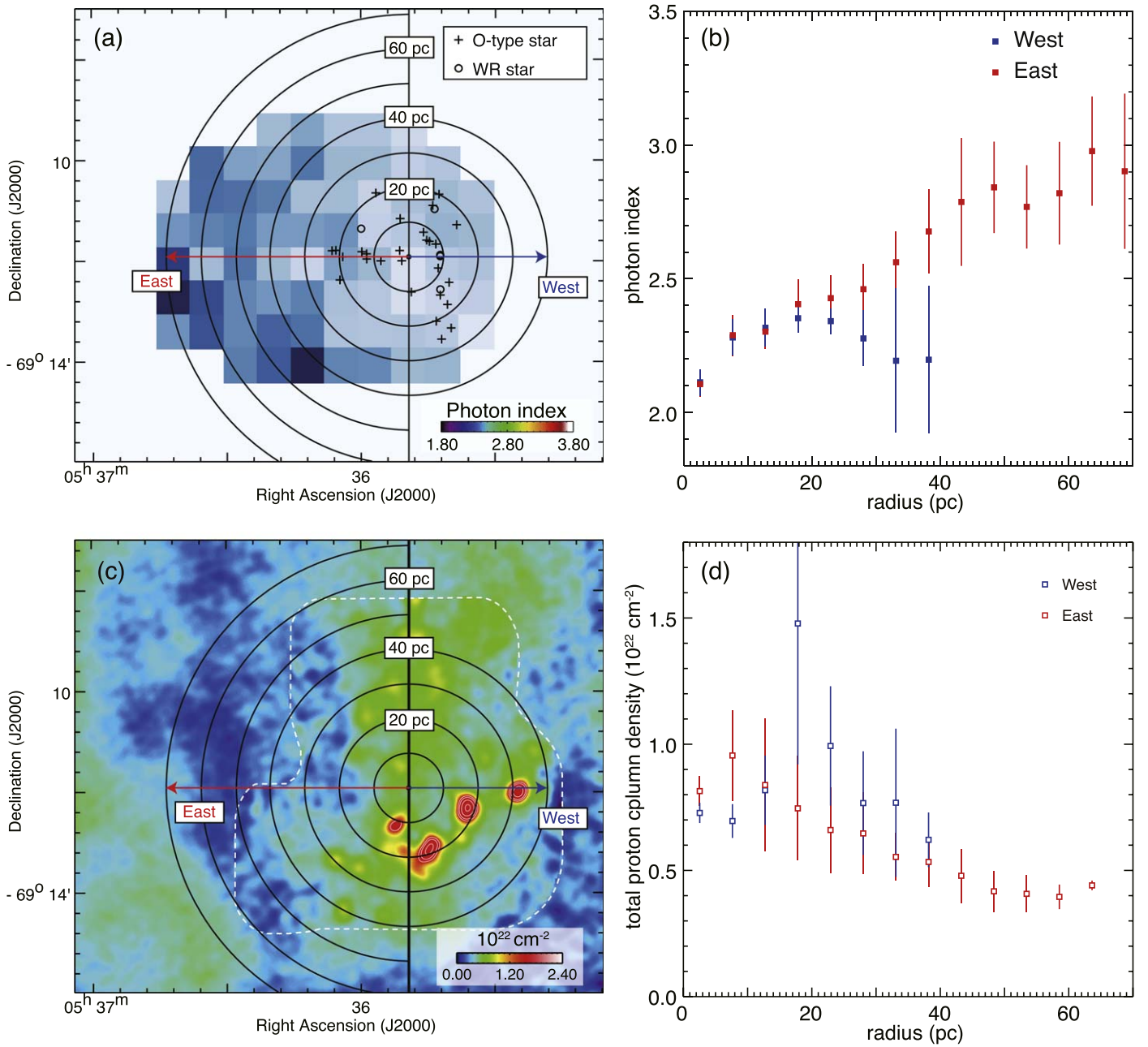


Figure 10. (a) Map of the photon index, which is the same as the image in Figure 6(a). Black crosses and circles indicate O-type stars and WR stars, respectively. (b) Western (blue) and eastern (red) radial profiles of the photon index centered on the center of mass of the high-mass stars. (c) Map of $N_p(\text{H}_2+\text{HI})$, which is the same as the image in Figure 5(c). (d) Western (blue) and eastern (red) radial profiles of $N_p(\text{H}_2+\text{HI})$ centered on the center of mass of the high-mass stars.

3. The X-ray photon index tends to become small toward the center of the high-mass star cluster, which suggests that the high-mass star cluster is responsible for the production of the cosmic-ray electrons via SNe. It is most likely that a single or multiple SNe occurred in the cluster, which accelerated cosmic-ray electrons via diffusive shock acceleration.
4. Fukui et al. (2017) presented a scenario where the HI colliding flow triggered the formation of R136 and the other surrounding high-mass stars. The HI velocity distribution shown in the present work suggests that 30 Dor C is located toward the merging area of the low velocity HI. The high-mass stars in 30 Dor C are part of these stars, which suggests that their formation is coeval

in the last few Myr. This formation may explain the multiple SNe that were suggested in Section 4.1.

We are grateful to the anonymous referee for their useful comments, which helped the authors to improve the paper. This paper makes use of the following ALMA data: ADS/JAO. ALMA#2013.1.01042.S and #2015.1.01232. ALMA is a partnership of ESO (representing its member states), NSF (USA) and NINS (Japan), together with NRC (Canada) and NSC and ASIAA (Taiwan) and KASI (Republic of Korea), in cooperation with the Republic of Chile. The Joint ALMA Observatory is operated by ESO, AUI/NRAO and NAOJ. This work made use of the XMM-Newton Extended Source Analysis Software. The Australia Telescope Compact Array,

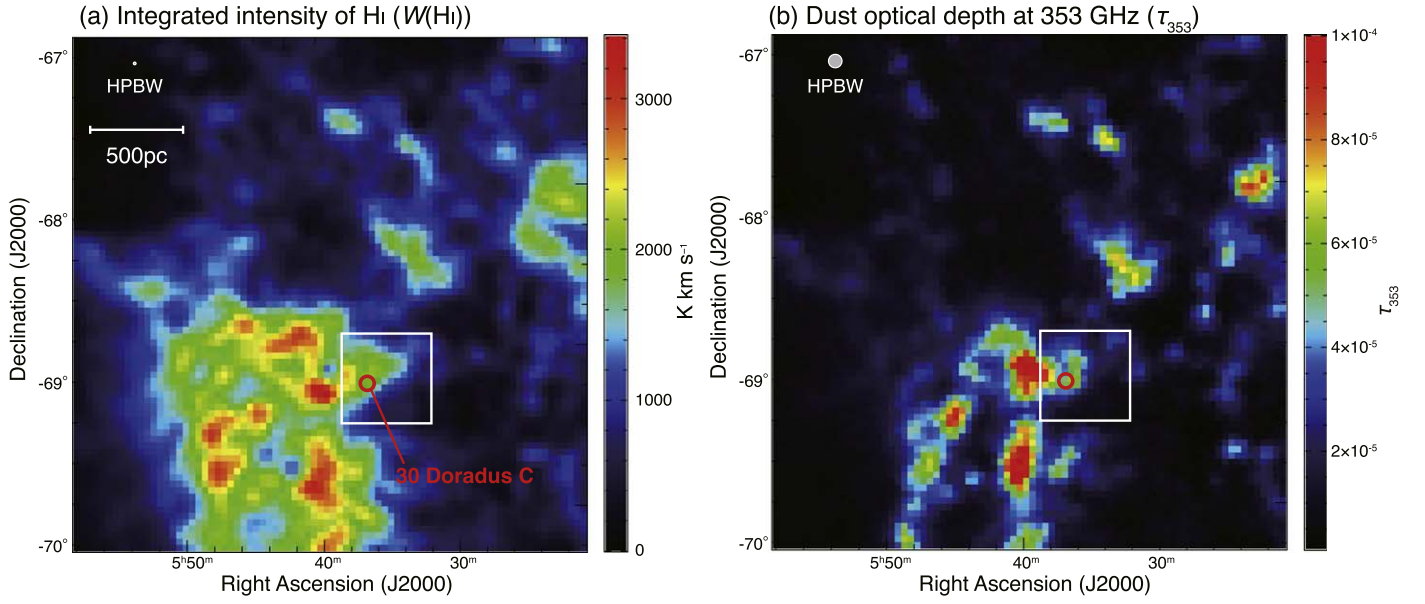


Figure 11. Maps of (a) integrated intensity of HI ($W(\text{HI})$) and (b) the dust optical depth at 353 GHz (τ_{353}) around 30 Dor C. The red circles indicate the positions of 30 Dor C. The white box is the $30' \times 30'$ region centered at $(\alpha_{J2000}, \delta_{J2000}) = (5^{\text{h}} 34^{\text{m}} 50^{\text{s}}, -69^{\circ} 13' 49'')$.

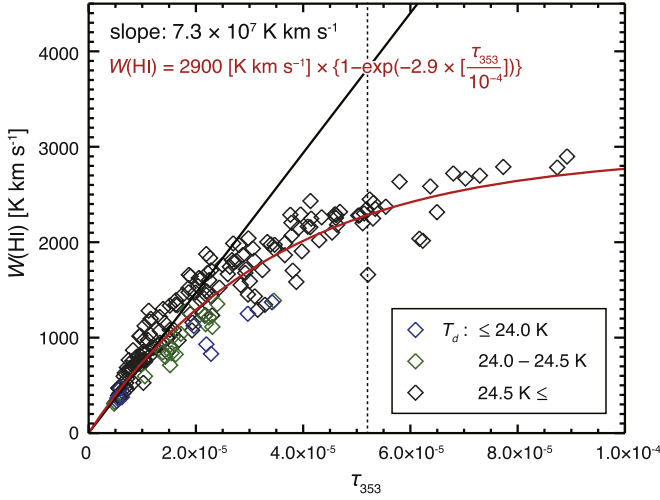


Figure 12. Scatter plot between $W(\text{HI})$ and τ_{353} in the region indicated as white boxes of Figure 11. We show three T_d ranges: 24.0 K and lower (blue), 24.0–24.5 K (green), and 24.5 K and higher (black). The black line denotes the result of the least-squares fitting of a straight line whose slope is indicated in the top left corner. The red curve is the function of Equation (11) with $a = 2900$ and $b = 2.9 \times 10^4$ (see the text). The black-dashed line represents $\tau_{353} = 5.2 \times 10^{-5}$, which is the typical value at the 30 Doradus C region.

and Parkes radio telescope are part of the ATNF which is funded by the Australian Government for operation as a National Facility managed by CSIRO. We acknowledge Kevin Grieve for his valuable support during the HI observations and data reduction. The ASTE telescope is operated by National Astronomical Observatory of Japan (NAOJ). This study was financially supported by Grants-in-Aid for Scientific Research (KAKENHI) of the Japanese Society for the Promotion of Science (JSPS, grant Nos. 15H05694, 16K17664, 19H05075, and 19K14758). K. Tokuda was supported by NAOJ ALMA Scientific Research grant No. 2016-03B.

Software: CASA (v 5.1.0; McMullin et al. 2007), MIRIAD (Sault et al. 1995), SAS (Gabriel et al. 2004), ESAS (Kuntz & Snowden 2008).

Appendix

Recent comparative studies between HI and dust emission have confirmed that a large amount of optically thick HI gas is associated with high-latitude clouds (e.g., Fukui et al. 2014, 2015; Okamoto et al. 2017; Hayashi et al. 2019a, 2019b). Fukui et al. (2015) concluded that the amount and distribution of the hydrogen gas could be estimated more accurately by using the scaling factor Equation (4) with $X \sim 2$. In this study, we estimate this scaling factor X for the 30 Dor C region using the integrated intensity of HI ($W(\text{HI})$) and the dust opacity at 353 GHz (τ_{353}) around 30 Dor C. Figure 11 shows the distributions of (a) $W(\text{HI})$ and (b) τ_{353} around 30 Dor C. $W(\text{HI})$ is the integrated intensity of HI, whose integration velocity range is from 150 to 350 km s^{-1} . The velocity range contains all of the interstellar gas of the LMC. We find that 30 Dor C is located at western edge of the HI Ridge.

Figure 12 shows a scatter plot between $W(\text{HI})$ and τ_{353} of the $30' \times 30'$ region around 30 Dor C (see white boxes of Figure 11). We find a non-linear relation when τ_{353} or $W(\text{HI})$ becomes larger value (see Figure 12). When the dust temperature (T_d) is high, the spin temperature of HI is thought to be also high and hence HI gas is expected to be optically thin. We estimated the $N_p(\text{HI})$ by the following equation under the assumption that HI gas is optically thin,

$$N_p(\text{HI}) = 1.823 \times 10^{18} \cdot W(\text{HI}). \quad (6)$$

The black line in Figure 12 represents the result of the least-squares fits using the data points of $T_d \geq 24.0$ K and $\tau_{353} < 1.5 \times 10^{-5}$ assuming zero intercept and the function is represented as Equation (7),

$$W(\text{HI}) = \tau_{353} \times 7.3 \times 10^7. \quad (7)$$

The relationship between $N_p(\text{HI})$ and τ_{353} is estimated at $T_d \geq 24.0$ K;

$$N_p(\text{HI}) = (1.3 \times 10^{26}) \times \tau_{353}, \quad (8)$$

where the slope of 1.3×10^{26} is calculated by using Equations (6) and (7). As mentioned by Fukui et al. (2014),

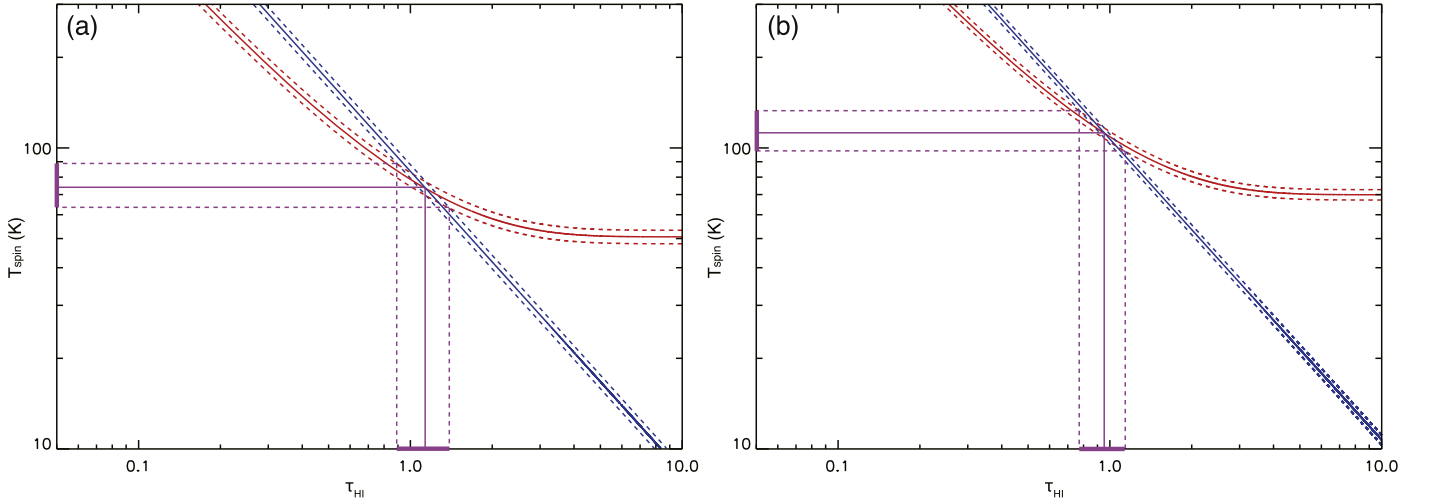


Figure 13. Estimations of T_s and τ_{HI} in the typical cases of (a) $T_s \sim 70$ K, and (b) ~ 110 K. Red and blue lines show Equations (7) and (8), respectively. The solution that satisfies both Equations (7) and (8) is the crossing point of the two lines. The dashed lines around each line indicate the error when taking observational parameters into consideration. The purple-solid lines represent the solutions of T_s and the dashed lines show their errors.

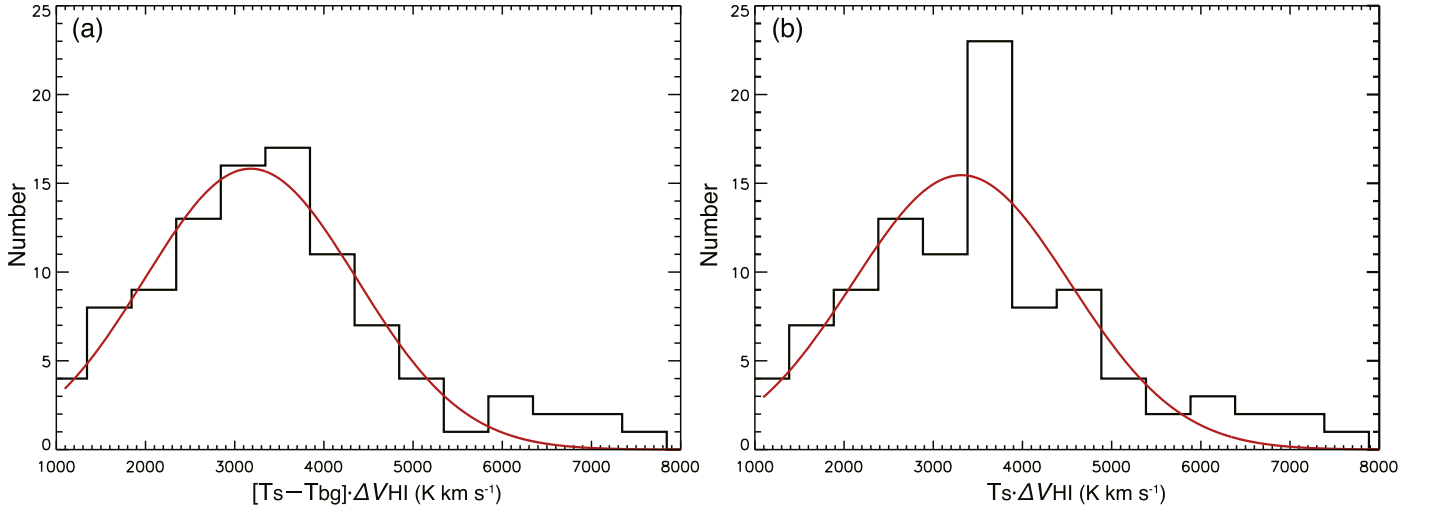


Figure 14. Histograms of (a) $[T_s - T_{\text{bg}}] \Delta V_{\text{HI}}$, and (b) $T_s \Delta V_{\text{HI}}$ at the region enclosed by white boxes of Figure 11. Red curves indicate the Gaussian functions fitted by these histograms. The peak values of these functions are (a) 3200 K km s⁻¹, and (b) 3300 K km s⁻¹.

relation (8) holds as long as the dust properties, such a gas-to-dust ratio, are uniform. In this case, it is possible to calculate $N_p(\text{HI})$ from τ_{353} using Equation (8). Then, the coupled Equations (9) and (10) in the following are used to solve for T_s and τ_{HI} ,

$$W(\text{HI}) = [T_s - T_{\text{bg}}] \cdot \Delta V_{\text{HI}} \cdot [1 - \exp(\tau_{\text{HI}})], \quad (9)$$

$$\tau_{\text{HI}} = \frac{N_p(\text{HI})}{1.823 \times 10^{18}} \cdot \frac{1}{T_s} \cdot \frac{1}{\Delta V_{\text{HI}}}. \quad (10)$$

Equations (9) and (10) lead to Equation (11),

$$W(\text{HI}) = a \cdot [1 - \exp(-b \cdot \tau_{353})], \quad (11)$$
















where $a = [T_s - T_{\text{bg}}] \cdot \Delta V_{\text{HI}}$ and $b = \frac{1.3 \times 10^{26}}{1.823 \times 10^{18}} \cdot \frac{1}{T_s} \cdot \frac{1}{\Delta V_{\text{HI}}}$. Here, τ_{HI} is the optically depth, and T_s is the spin temperature. T_{bg} is brightness temperature of background and we assume $T_{\text{bg}} = 2.7$ K taking the effect of cosmic microwave background into account. ΔV_{HI} is the HI line width given by $W(\text{HI})/(\text{peak HI brightness temperature})$.

The red curve in Figure 12 is derived by the least-squares fits using all data points. This function represents the Equation (11) with $a = 2900$ and $b = 2.9 \times 10^4$. The black-dashed line in Figure 12 indicates the mean value of $\tau_{353} = 5.2 \times 10^{-5}$ in 30 Dor C. By adopting the value into curve functions, we derived $W(\text{HI}) = 3800$ K km s⁻¹ for the black-line function, and $W(\text{HI}) = 2250$ K km s⁻¹ for the red-curve function. This result means that the column density of HI gas calculated by using Equation (6) is estimated to be smaller than that of expected value. Thus, we estimated the scaling factor $X = 3800/2250 \sim 1.7$ in the Equation (4).

Using Equations (9) and (10), T_s was solved by the bisection method at each data point. The two relations in the T_s - τ_{HI} plane for two typical value of (a) $T_s \sim 70$ K and (b) $T_s \sim 110$ K are shown in Figure 13. Figure 13 also shows the errors in T_s and τ_{HI} , which were estimated from the 1σ noise level of the observation data of HI and τ_{353} . We estimate the error ranges in Figure 13 as follows : (a) $T_s \sim 70^{+20}_{-13}$ K, $\tau_{\text{HI}} \sim 1.14^{+0.25}_{-0.24}$, (b) $T_s \sim 110^{+25}_{-18}$ K, $\tau_{\text{HI}} \sim 0.96^{+0.18}_{-0.18}$. The equations give the solutions with ~ 20 – 30% errors. Figure 14 shows the histogram of (a) $[T_s - T_{\text{bg}}] \cdot \Delta V_{\text{HI}}$ and (b) $T_s \cdot \Delta V_{\text{HI}}$ given by using the ΔV_{HI}

and the solutions of T_s at each data point. The red curves in Figures 14(a) and (b) represent the results of the Gaussian fitting using those histograms. We estimate $a = 3200$ and $b = 2.2 \times 10^4$ from these mean values of the Gaussian functions. When $a = 3200$ and $b = 2.2 \times 10^4$ are substituted into Equation (11), $W(\text{HI}) = 2200 \text{ K km s}^{-1}$ by adopting $\tau_{353} = 5.2 \times 10^{-5}$, which is the mean value in 30 Dor C. In this case, the scaling factor $X \sim 1.7$ in Equation (4) is the same as the estimation by the red-curve function in Figure 12. Accordingly, we estimated the amount of the HI gas more accurately using the scaling factor $X \sim 1.7$ in Equation (4) in the present study.

ORCID iDs

Y. Yamane  <https://orcid.org/0000-0001-8296-7482>
H. Sano  <https://orcid.org/0000-0003-2062-5692>
M. D. Filipović  <https://orcid.org/0000-0002-4990-9288>
K. Tokuda  <https://orcid.org/0000-0002-2062-1600>
F. Aharonian  <https://orcid.org/0000-0003-1157-3915>
S. Inutsuka  <https://orcid.org/0000-0003-4366-6518>
N. Maxted  <https://orcid.org/0000-0003-2762-8378>
T. Onishi  <https://orcid.org/0000-0001-7826-3837>
G. Rowell  <https://orcid.org/0000-0002-9516-1581>
K. Tsuge  <https://orcid.org/0000-0002-2794-4840>
S. Yoshiike  <https://orcid.org/0000-0002-2458-7876>
A. Kawamura  <https://orcid.org/0000-0001-7813-0380>
A. Bamba  <https://orcid.org/0000-0003-0890-4920>
K. Tachihara  <https://orcid.org/0000-0002-1411-5410>
Y. Fukui  <https://orcid.org/0000-0002-8966-9856>

References

- Abbott, D. C. 1982, *ApJ*, **263**, 723
Babazaki, Y., Mitsuishi, I., Matsumoto, H., et al. 2018, *ApJ*, **864**, 12
Bamba, A. 2004, PhD Thesis, Kyoto Univ. Japan
Bamba, A., Ueno, M., Nakajima, H., & Koyama, K. 2004, *ApJ*, **602**, 257
Bamba, A., Yamazaki, R., Yoshida, T., et al. 2005, *ApJ*, **621**, 793
Bekki, K., & Chiba, M. 2007, *MNRAS*, **381**, L16
Bolatto, A. D., Wolfire, M., & Leroy, A. K. 2013, *ARA&A*, **51**, 207
Bonanos, A. Z., Massa, D. L., Sewilo, M., et al. 2009, *AJ*, **138**, 1003
Bozzetto, L. M., Filipović, M. D., Vukotić, B., et al. 2017, *ApJS*, **230**, 2
Chu, Y.-H., & Mac Low, M.-M. 1990, *ApJ*, **365**, 510
Cornwell, T. J. 2008, *ISTSP*, **2**, 793
Dennerl, K., Haberl, F., Aschenbach, B., et al. 2001, *A&A*, **365**, L202
Dickey, J. M., & Lockman, F. J. 1990, *ARA&A*, **28**, 215
Ezawa, H., Kawabe, R., Kohno, K., & Yamamoto, S. 2004, *Proc. SPIE*, **5489**, 763
Fujimoto, M., & Noguchi, M. 1990, *PASJ*, **42**, 505
Fukui, Y., Kawamura, A., Minamidani, T., et al. 2008, *ApJS*, **178**, 56
Fukui, Y., Okamoto, R., Kaji, R., et al. 2014, *ApJ*, **796**, 59
Fukui, Y., Torii, K., Onishi, T., et al. 2015, *ApJ*, **798**, 6
Fukui, Y., Tsuge, K., Sano, H., et al. 2017, *PASJ*, **69**, L5
Fukui, Y., Torii, K., Hattori, Y., et al. 2018, *ApJ*, **859**, 166
Gabriel, C., Denby, M., Fyfe, D. J., et al. 2004, ASP Conf. Ser., 314, Astronomical Data Analysis Software and Systems (ADASS) XIII (San Francisco, CA: ASP), 759
Hayashi, K., Okamoto, R., Yamamoto, H., et al. 2019a, *ApJ*, **878**, 131
Hayashi, K., Mizuno, T., Fukui, Y., et al. 2019b, *ApJ*, **884**, 130
H.E.S.S. Collaboration, Abramowski, A., Aharonian, F., et al. 2015, *Sci*, **347**, 406
Inoue, T., Yamazaki, R., & Inutsuka, S. 2009, *ApJ*, **695**, 825
Inoue, T., Yamazaki, R., Inutsuka, S., et al. 2012, *ApJ*, **744**, 71
Kavanagh, P. J., Sasaki, M., Bozzetto, L. M., et al. 2015, *A&A*, **573**, A73
Kavanagh, P. J., Vink, J., Sasaki, M., et al. 2019, *A&A*, **621**, A138
Kim, S., Staveley-Smith, L., Dopita, M. A., et al. 2003, *ApJS*, **148**, 473
Kuntz, K. D., & Snowden, S. L. 2008, *A&A*, **478**, 575
Le Mame, A. E. 1968, *MNRAS*, **139**, 461
Long, K. S., Helfand, D. J., & Grabelsky, D. A. 1981, *ApJ*, **248**, 925
Lopez, L. A., Grefenstette, B. W., Auchettl, K., et al. 2020, *ApJ*, **893**, 144
Luks, T., & Rohlfs, K. 1992, *A&A*, **263**, 41
McMullin, J. P., Waters, B., Schiebel, D., Young, W., & Golap, K. 2007, ASP Conf. Ser. 376, Astronomical Data Analysis Software and Systems XVI (Tucson, AZ: ASP), 127
Mills, B. Y., Turtle, A. J., Little, A. G., et al. 1984, *AuJPh*, **37**, 321
Minamidani, T., Tanaka, T., Mizuno, Y., et al. 2011, *AJ*, **141**, 73
Okamoto, R., Yamamoto, H., Tachihara, K., et al. 2017, *ApJ*, **838**, 132
Pietrzyński, G., Graczyk, D., Gieren, W., et al. 2013, *Natur*, **495**, 76
Planck Collaboration, Abergel, A., Ade, P. A. R., et al. 2014, *A&A*, **571**, A11
Sano, H., Fukuda, T., Yoshiike, S., et al. 2015, *ApJ*, **799**, 175
Sano, H., Inoue, T., Tokuda, K., et al. 2020, *ApJL*, **904**, L24
Sano, H., Reynoso, E. M., Mitsuishi, I., et al. 2017, *JHEAp*, **15**, 1
Sano, H., Sato, J., Horachi, H., et al. 2010, *ApJ*, **724**, 59
Sano, H., Tanaka, T., Torii, K., et al. 2013, *ApJ*, **778**, 5975
Sano, H., Yamane, Y., Voisin, F., et al. 2017, *ApJ*, **843**, 61
Sault, R. J., Teuben, P. J., & Wright, M. C. H. 1995, ASP Conf. Ser. 77, Astronomical Data Analysis Software and Systems IV (San Francisco, CA: ASP), 433
Smith, D. A., & Wang, Q. D. 2004, *ApJ*, **611**, 881
Sorai, K., Nakai, N., Kuno, N., Nishiyama, K., & Hasegawa, T. 2000, *PASJ*, **52**, 785
Testor, G., Schild, H., & Lortet, M. C. 1993, *A&A*, **280**, 426
Tsuge, K., Sano, H., Tachihara, K., et al. 2019, *ApJ*, **871**, 44
Uchiyama, Y., Aharonian, F. A., Tanaka, T., et al. 2007, *Natur*, **449**, 576
Weaver, R., McCray, R., Castor, J., et al. 1977, *ApJ*, **218**, 377
Yamaguchi, H., Bamba, A., & Koyama, K. 2009, *PASJ*, **61**, S175
Zirakashvili, V. N., & Aharonian, F. 2007, *A&A*, **465**, 695